

## Candidate Members of the VMP/EMP Disk System of the Galaxy from the SkyMapper and SAGES Surveys

JIHYE HONG <sup>1,2</sup> TIMOTHY C. BEERS <sup>1,2</sup> YOUNG SUN LEE <sup>3,1</sup> YANG HUANG <sup>4,5</sup> YUTAKA HIRAI <sup>1,6,2,\*</sup>  
JONATHAN CABRERA GARCIA <sup>1,2</sup> DEREK SHANK <sup>1,2</sup> SHUAI XU <sup>7,8</sup> MOHAMMAD K. MARDINI <sup>9,10,11</sup>  
THOMAS CATAPANO <sup>1,2</sup> GANG ZHAO <sup>5</sup> ZHOU FAN <sup>5</sup> JIE ZHENG <sup>5</sup> WEI WANG <sup>5</sup> KEFENG TAN <sup>5</sup> JINGKUN ZHAO <sup>5</sup>  
AND CHUN LI <sup>5</sup>

<sup>1</sup>Department of Physics and Astronomy, University of Notre Dame, Notre Dame, IN 46556, USA

<sup>2</sup>Joint Institute for Nuclear Astrophysics – Center for the Evolution of the Elements (JINA-CEE), USA

<sup>3</sup>Department of Astronomy and Space Science, Chungnam National University, Daejeon 34134, Republic of Korea

<sup>4</sup>School of Astronomy and Space Science, University of Chinese Academy of Sciences, Beijing 100049, People’s Republic of China

<sup>5</sup>CAS Key Lab of Optical Astronomy, National Astronomical Observatories, Chinese Academy of Sciences, Beijing 100101, People’s Republic of China

<sup>6</sup>Astronomical Institute, Tohoku University, 6-3 Aoba, Aramaki, Aoba-ku, Sendai, Miyagi 980-8578, Japan

<sup>7</sup>Institute for Frontiers in Astronomy and Astrophysics, Beijing Normal University, Beijing 102206, China

<sup>8</sup>Department of Astronomy, Beijing Normal University, Beijing, 100875, P.R.China

<sup>9</sup>Department of Physics, Zarqa University, Zarqa 13110, Jordan

<sup>10</sup>Kavli IPMU (WPI), UTIAS, The University of Tokyo, Kashiwa, Chiba 277-8583, Japan

<sup>11</sup>Institute for AI and Beyond, The University of Tokyo 7-3-1 Hongo, Bunkyo-ku, Tokyo 113-8655, Japan

Submitted to ApJS

### Abstract

Photometric stellar surveys now cover a large fraction of the sky, probe to fainter magnitudes than large-scale spectroscopic studies, and are relatively free from the target-selection biases often associated with such studies. Photometric-metallicity estimates that include narrow/medium-band filters can achieve comparable accuracy and precision to existing low- and medium-resolution spectroscopic surveys such as SDSS/SEGUE and LAMOST, with metallicities as low as  $[\text{Fe}/\text{H}] \sim -3.5$  to  $-4.0$ . Here we report on an effort to identify likely members of the Galactic disk system among the Very Metal-Poor (VMP;  $[\text{Fe}/\text{H}] \leq -2$ ) and Extremely Metal-Poor (EMP;  $[\text{Fe}/\text{H}] \leq -3$ ) stars. Our analysis is based on a sample of some 11.5 million stars with full space motions selected from the SkyMapper Southern Survey (SMSS) and Stellar Abundance and Galactic Evolution Survey (SAGES). After applying a number of quality cuts, designed to obtain the best available metallicity and dynamical estimates, we analyze a total of about 7.74 million stars in the combined SMSS/SAGES sample. We employ two techniques which, depending on the method, identify between 5,878 and 7,600 VMP stars (19% to 25% of all VMP stars) and between 345 and 399 EMP stars (35% to 40% of all EMP stars) that appear to be members of the Galactic disk system on highly prograde orbits ( $v_\phi > 150 \text{ km s}^{-1}$ ), the majority of which have low orbital eccentricities ( $\text{ecc} \leq 0.4$ ). The large fractions of VMP/EMP stars that are associated with the MW disk system strongly suggests the presence of an early forming “primordial” disk.

**Keywords:** Milky Way dynamics (1051), Galaxy dynamics (591), Galactic Archaeology (2178), Milky Way evolution (1052), Milky Way formation (1053)

### 1. INTRODUCTION

Over the past few decades, large-scale spectroscopic surveys such as the HK Survey (Beers et al. 1985, 1992), the Hamburg/ESO Survey (Christlieb 2003), SDSS (York et al. 2000), SEGUE (Yanny et al. 2009; Rockosi et al. 2022),

RAVE (Steinmetz et al. 2006), LAMOST (Deng et al. 2012; Zhao et al. 2012), GALAH (De Silva et al. 2015), APOGEE (Majewski et al. 2017), the H3 Survey (Conroy et al. 2019), and the *Gaia* mission (Gaia Collaboration et al. 2023) have changed the paradigm of observational studies by providing detailed chemical and kinematic information for numerous stars in the Milky Way (MW), in particular for the relatively

\* JSPS Research Fellow

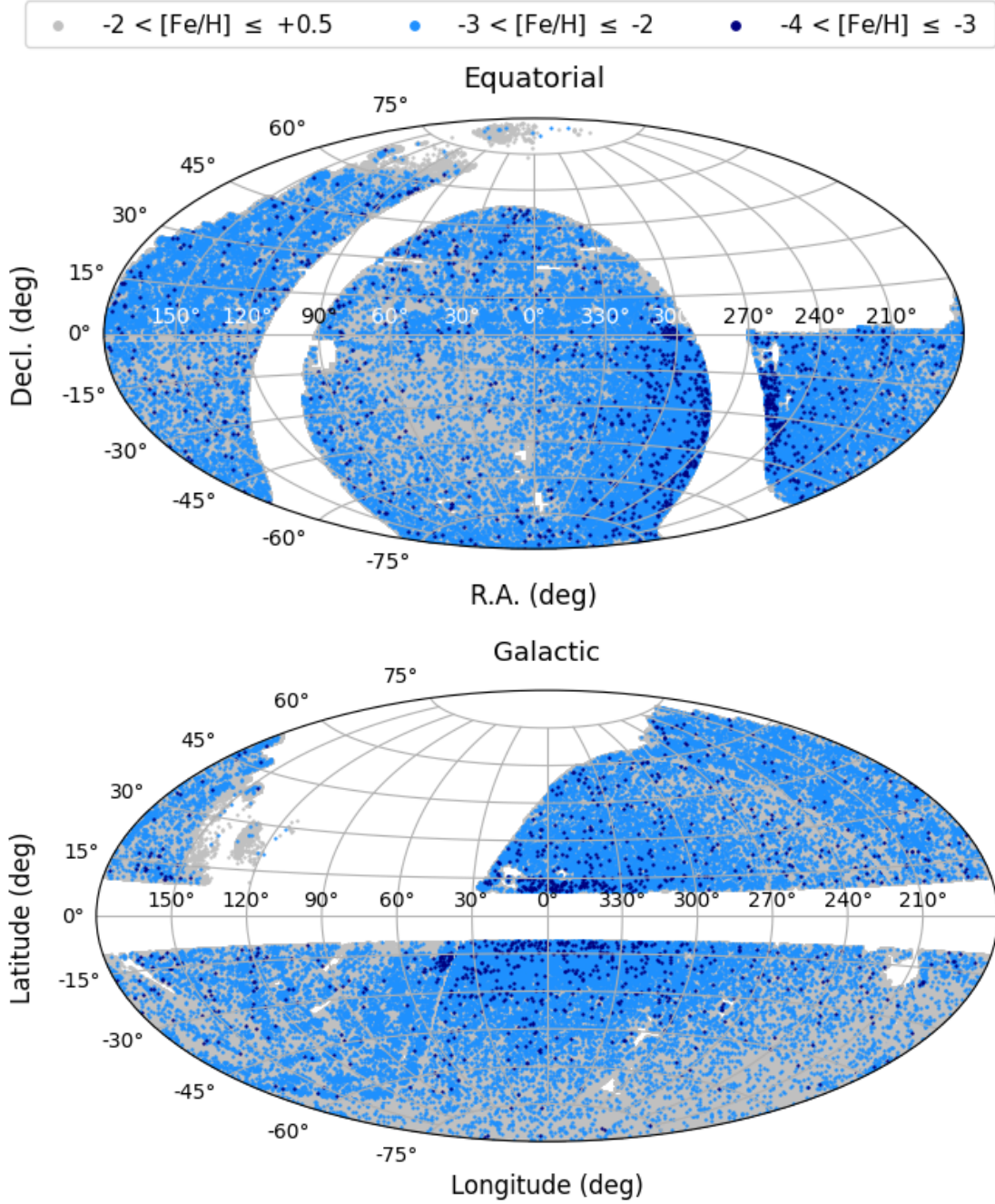


**Figure 1.** Mollweide projection of the positions for some 8 million stars selected from the Southern (SMSS) and Northern (SAGES) photometric surveys, in equatorial (top panel) and Galactic (bottom panel) coordinates. These stars all have available metallicity estimates, based on calibrated  $u - G_{\text{BP}}$  colors and  $v - G_{\text{BP}}$  colors, a combination of the  $u/v$ -bands from SMSS/SAGES and the ultra wide-band *Gaia*  $G_{\text{BP}}$  prism spectra (Huang et al. 2022, 2023). See the Appendix for a discussion of the cuts that are applied to the sample prior to assigning final metallicities. The gray-filled circles indicate the stars with derived metallicities in the range  $-2 < [\text{Fe}/\text{H}] \leq +0.5$ , the light blue-filled circles are stars with  $-3 < [\text{Fe}/\text{H}] \leq -2$ , and the dark blue-filled circles are stars with  $-4 < [\text{Fe}/\text{H}] \leq -3$ . The stars shown all have available radial velocities and astrometric information. For the purpose of our analysis, we exclude stars identified as likely binaries by Huang et al. (2022, 2023), cool dwarfs ( $T_{\text{eff}} < 4,500$  K), and likely members of recognized globular clusters. For stars in common between the two surveys, we have used the average value of the photometric-metallicity estimates.

rare very metal-poor (VMP;  $[\text{Fe}/\text{H}] \leq -2$ ) and extremely metal-poor (EMP;  $[\text{Fe}/\text{H}] \leq -3$ ) stars.

Whether performed based on spectroscopic follow-up of metal-poor candidates from objective-prism surveys, or broad-band photometric surveys such as SDSS/SEGUE or Pan-STARRS (Chambers et al. 2016), it is challenging to avoid target-selection biases that can confound the interpretation of the relative contributions of stars of different metallicity to the recognized Galactic components. In addition, the first step in surveys dedicated to finding low-metallicity stars is often to limit the regions of the sky under consideration to higher Galactic latitude (e.g.,  $|b| > 30^\circ$ ), precluding identification of substantial numbers of VMP/EMP stars in the disk system of the MW.

In a series of recent papers, An & Beers (2020, 2021a,b) and An et al. (2023) have constructed “blueprints” of the MW’s stellar populations from analysis of the orbital rotation (inferred from proper motions and distance estimates alone) as a function of carefully calibrated photometric-metallicity estimates for stars with available broad-band *ugriz* from SDSS/SEGUE and other surveys. This approach has proven quite powerful. Among other results, these authors have confirmed the presence of the inner- and outer-halo populations, and demonstrated that the metal-weak thick disk (MWTD) is a separable population from the canonical thick disk (also shown by Carollo et al. 2019), and identified other previously known structures. In addition, they identified a continuous sequence of stars in the rotational velocity vs. metallicity space that may be associated with a starburst event when the earlier disk system encountered *Gaia*-Sausage-Enceladus (GSE). Evidence for this starburst event is also reported in Lee et al. (2023).

Over the past few years, photometric surveys based on combinations of narrow-band and medium- to broad-band filters have been (or are being) executed (e.g., SkyMapper; Keller et al. 2007, the Pristine Survey; Starkenburg et al. 2017, SAGES; Zheng et al. 2018, J-PLUS; Cenarro et al. 2019, and S-PLUS; Mendes de Oliveira et al. 2019). Typically, such surveys do not avoid regions of the MW at lower Galactic latitudes, other than those limited by very high interstellar extinction and reddening or crowding. As a result, VMP/EMP stars in the MW’s disk system have been increasingly discovered, though their numbers are still relatively small.

From a number of the above surveys, recent papers have provided identifications of VMP/EMP (and in a handful of cases, ultra metal-poor, UMP;  $[\text{Fe}/\text{H}] \leq -4$ ) stars in the MW with disk-like orbits, based on medium-resolution, and in some cases high-resolution, spectroscopic follow-up (see, e.g., Sestito et al. 2019, 2020; Di Matteo et al. 2020; Venn et al. 2020; Carter et al. 2021; Cordoni et al. 2021;

Fernández-Alvar et al. 2021; Mardini et al. 2022a,b; Carollo et al. 2023, and references therein).

The SkyMapper Southern Survey Data Release 2 (SMSS DR2; Onken et al. 2019) was carefully re-calibrated by Huang et al. (2021), and used by Huang et al. (2022) to derive stellar parameters, luminosity classifications, and metallicity estimates for over 24 million stars in the Southern Hemisphere, based on colors formed by combinations of the SMSS narrow/medium-band *u* and *v* filter magnitudes and the  $G_{\text{BP}}$  magnitude obtained from the ultra wide-band prism spectra from *Gaia*.

The recently completed Stellar Abundance and Galactic Evolution Survey (SAGES; Fan et al. 2023), which employs similar, but not identical, filters to SMSS, has been similarly adopted by Huang et al. (2023) to obtain stellar parameters, luminosity classifications, and metallicity estimates for nearly 26 million stars in the Northern Hemisphere.

Here we identify 7,635 VMP and 402 EMP candidate stars with disk-like orbits populating the rapidly rotating disk system of the MW ( $v_\phi > 150 \text{ km s}^{-1}$ ), selected from a subset of roughly 11.5 million stars from the SMSS and SAGES photometric surveys with available radial velocities (RVs), proper motions, and other astrometric data from which full space motions are derived. We approximately separate stars with disk-like from halo-like orbits by two criteria that have been commonly used in the literature, then consider their relative fractions at low metallicities.

This paper is organized as follows. Section 2 describes the data sets we employ and the choices made for the adopted metallicity estimates, as well as the derivation of dynamical parameters. In this section, we also describe two methods that have been commonly used to identify stars with potential disk-like orbits. Section 3 presents maps of the orbital rotational velocities of the stars as a function of  $[\text{Fe}/\text{H}]$ , where potential VMP/EMP candidates with disk-like orbits can already be seen, and compare their relative fractions as a function of  $[\text{Fe}/\text{H}]$ . Section 4 presents a discussion, along with conjectures on the origins of VMP/EMP disk-like stars based on interpretations from numerical simulations. We conclude with a summary and future prospects in Section 5.

## 2. DATA AND METHODS

### 2.1. Data

Huang et al. (2022) derived stellar parameters, including metallicity estimates, for more than 19 million dwarfs and 5 million giants over essentially the entire Southern Hemisphere from SMSS DR2, including about 704,000 VMP and 27,000 EMP stars. If we restrict their sample to stars with available RVs from *Gaia* DR3 (Gaia Collaboration et al. 2023) and other sources, the number of stars is about 7.4 million, including roughly 54,000 VMP and 2,300 EMP stars.

SAGES observed slightly less than half of the Northern Hemisphere. Notably, SAGES did not cover a large fraction of the North Galactic Pole (NGP), while SMSS covered the entire South Galactic Pole (SGP). Another crucial difference between SAGES and SMSS is that the central wavelength of the SAGES  $v$ -band filter is shifted redward relative to the SMSS  $v$ -band filter by about 110 Å, so it fully includes the region of the Ca II H & K lines (Zheng et al. 2018). Huang et al. (2023) use a similar approach to Huang et al. (2022), and obtained effective temperatures, luminosity classifications based on surface gravity, and metallicity estimates for over 26 million stars, including some 861,000 VMP and 13,000 EMP stars from SAGES DR1 (Fan et al. 2023). About 4.1 million stars in this catalog have available RVs, including roughly 39,000 VMP and 1,900 EMP stars.

For this study, we begin with a sample of about 7.4 million stars from SMSS and 4.1 million stars from SAGES with available RVs, proper motions, and distance estimates, as provided in the catalogs from Huang et al. (2022) and Huang et al. (2023), respectively. After combining these data sets, binary stars photometrically classified by Huang et al. (2022, 2023) and cool dwarfs ( $T_{\text{eff}} < 4,500$  K) have been removed. We also removed about 1,500 likely stellar globular cluster members based on the catalogs of Harris (2010)<sup>1</sup> and Baumgardt & Vasiliev (2021).

Metallicity estimates for the stars in our sample are based on calibrated  $u - G_{\text{BP}}$  colors and  $v - G_{\text{BP}}$  colors, a combination of the  $u/v$ -bands from SMSS/SAGES and the ultra wide-band *Gaia*  $G_{\text{BP}}$  prism spectra (Huang et al. 2022, 2023). As has been noted previously, the colors involving the  $u$ -band have a greater sensitivity to the presence of enhanced carbon in a star than those involving the  $v$ -band. For this reason, and in order to provide the best available metallicities, we do not include stars for which only  $u$ -band metallicity estimates are available, and those that have a difference between the  $u$ -band and  $v$ -band based abundances greater than 0.5 dex. See the Appendix for a justification, and full discussion of the cuts that are applied to the sample prior to assigning final adopted metallicities.

Figure 1 shows the sky distribution in equatorial and Galactic coordinates of about the 8 million numbers of combined sample, with symbols indicating the metallicity ranges of these stars. Note that for the  $\sim 185,000$  stars in common between the two surveys, we have calculated an average photometric-metallicity estimate.

Figure 2 shows the distribution of the errors in the photometric-metallicity estimates ( $\delta[\text{Fe}/\text{H}]$ ) for stars in the final sample of SMSS/SAGES stars, after we excluded the stars that have adopted photometric-metallicity errors greater than 0.5 dex. The left, middle, and right panels provide the

results for the sub-samples of stars with  $[\text{Fe}/\text{H}] \leq -1$ ,  $\leq -2$ , and  $\leq -3$ , respectively. The legends in each panel indicate the median errors for all stars in the listed metallicity range, and the errors for stars classified as dwarfs and giants. As can be seen, the errors increase with decreasing metallicity, as expected, but still remain reasonably low (median errors on the order of 0.1 to 0.2 dex). Note that these numbers refer to internal errors; external errors are somewhat larger, on the order of 0.25 to 0.35 dex (see the discussion in the Appendix).

## 2.2. Dynamical Parameters

The orbital parameters for the stars in our combined sample are determined using their 6D astrometric parameters (positions, RVs, proper motions, and distance estimates from Huang et al. 2022, 2023), and their corresponding errors, as inputs to the Action-based Galaxy Modelling Architecture<sup>2</sup> (AGAMA) package (Vasiliev 2019), adopting the Solar positions and peculiar motions described in Shank et al. (2022)<sup>3</sup>, and the gravitational potential MW2017 (McMillan 2017).

Similar to Shank et al. (2022), we input quantities through the orbital-integration process in AGAMA to calculate the cylindrical velocities ( $v_r$ ,  $v_\phi$ ,  $v_z$ ), cylindrical actions ( $J_r$ ,  $J_\phi$ ,  $J_z$ ), orbital specific energy ( $E$ ),  $r_{\text{apo}}$ ,  $r_{\text{peri}}$ , eccentricity ( $\text{ecc}$ ),  $Z_{\text{max}}$  (the maximum orbital distances reached by stars from the Galactic plane), and  $R_{\text{max}}$  (the maximum apocentric distance projected onto the Galactic plane), along with their associated errors<sup>4</sup>. Stars that were possibly unbound ( $E > 0 \text{ km}^2 \text{ s}^{-2}$ ) were identified and removed. This resulted in a total of 10.8 million stars in the SMSS/SAGES sample suitable for our kinematic analysis.

For our present purpose, we only included stars having derived errors less than 25 km/s in their orbital rotation velocities, and relative errors  $\leq 30\%$  in  $Z_{\text{max}}$  and  $R_{\text{max}}$ , which removed a total of about 239,000 stars from the combined sample. Moreover, in order to diminish the effect of reddening on the derived metallicities (of particular importance for stars near the disk), we only included stars with  $E(B - V) \leq 0.3$ , excluding a total of about 0.24 million stars, which includes roughly 8% and 15% of the total number of VMP and EMP stars, respectively. This produced a final sample of approximately 7.74 million stars (5.29 million SMSS stars and 2.45

<sup>2</sup> <http://github.com/GalacticDynamics-Oxford/Agama>

<sup>3</sup> We adopt a Solar position of  $(-8.249, 0, 0)$  kpc (GRAVITY Collaboration et al. 2020) and Solar peculiar motion  $(U, V, W)$ , about the Local Standard of Rest (LSR), as  $(11.1, 12.24, 7.25) \text{ km s}^{-1}$  (Schönrich et al. 2010), where  $V_{\text{LSR}} = 238.5 \text{ km s}^{-1}$ , defined as  $V_{\text{LSR}} = V_\odot - V$  and  $V_\odot = 250.70 \text{ km s}^{-1}$ , determined from Reid & Brunthaler (2020) based on our choice of Solar position and using the proper motion of the center of the Galaxy (Srg A\*) of  $-6.411 \text{ mas yr}^{-1}$ .

<sup>4</sup> Due to the very large number of stars in our sample, we estimated errors on  $R_{\text{max}}$ , unlike for the other dynamical parameters, by running the input quantities and their errors 50 times through AGAMA using a random sample of 10,000 stars, and assume that the relative errors apply to all stars.

<sup>1</sup> <https://physics.mcmaster.ca/~harris/mwgc.dat>



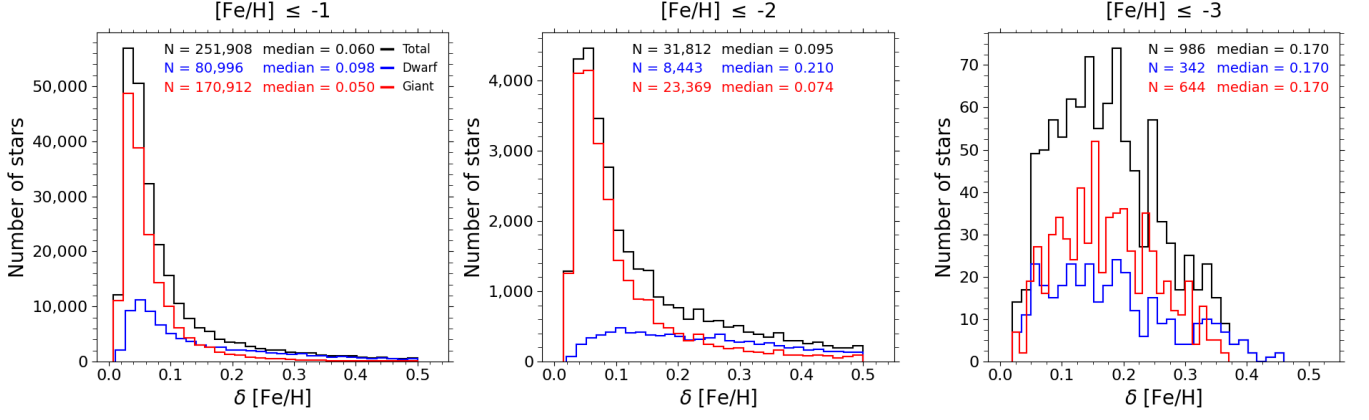


**Figure 2.** Histogram of the errors in metallicity ( $\delta$  [Fe/H]) for the final SMSS/SAGES sample. From left to right, the panels correspond to the MP ( $[\text{Fe}/\text{H}] \leq -1$ ), VMP ( $[\text{Fe}/\text{H}] \leq -2$ ), and EMP ( $[\text{Fe}/\text{H}] \leq -3$ ) sub-samples, respectively. The black, blue, and red histograms represent the total, dwarf, and giant stars in each metallicity range, respectively. The number of stars and the median values of  $\delta$  [Fe/H] are indicated in the legend of each panel.

million SAGES stars, which we refer to as the SMSS/SAGES sample hereafter).

### 2.3. Separation of Disk and Halo Stars

Previous analyses of the nature of stellar orbits in the MW have used a variety of techniques to separate stars on disk-like from halo-like orbits. Two simple approaches are described below.

#### 2.3.1. Maximum Height of Orbits

This approach, employed by Beers et al. (2014), Sestito et al. (2020, 2021), Limberg et al. (2021), and Mardini et al. (2022a), identifies stars in the disk-like and halo-like dynamical populations by assigning stars with  $Z_{\text{max}} \leq 3$  kpc to disk-like orbits and those with  $Z_{\text{max}} > 3$  kpc to halo-like orbits. Often, an additional criterion is adopted to identify the stars in the disk system by demanding that they be on highly prograde orbits. We follow a similar approach as described below, with a further division of the stars on disk-like orbits into those with  $Z_{\text{max}} \leq 1$  kpc, in an attempt to identify possible VMP/EMP thin-disk stars.

#### 2.3.2. “Wedges” in the Haywood Diagram

Following Haywood et al. (2018), we have also used plots of  $Z_{\text{max}}$  vs.  $\arctan(Z_{\text{max}}/R_{\text{max}})$ , which redistributes our sample stars into discrete wedges, corresponding to different dynamical populations, a method also employed by Schuster et al. (2012), Di Matteo et al. (2020), Kim et al. (2021), and Koppelman et al. (2021).

Here,  $R_{\text{max}}$  is defined as the projection of  $r_{\text{apo}}$  onto the Galactic plane, via the simple geometric relationship  $R_{\text{max}} = \sqrt{r_{\text{apo}}^2 - Z_{\text{max}}^2}$ . Note that, for simplicity of notation, below we define an “inclination angle” ( $IA$ ) to represent  $\arctan(Z_{\text{max}}/R_{\text{max}})$ . It should be kept in mind that  $Z_{\text{max}}$  and  $R_{\text{max}}$  are derived from the full ensemble of orbits traced by a

given star, so their  $IA$  is representative of that complete set, not a single orbit or an average of the orbits.

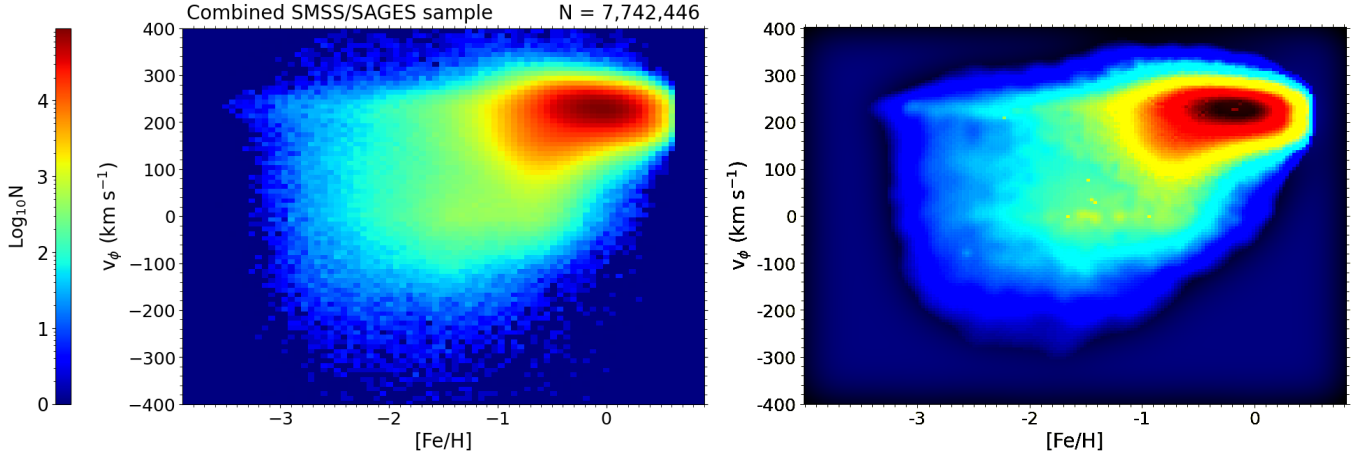
## 3. RESULTS

In this section, we identified about 31,800 VMP/EMP stars from the rotational velocity distribution of the final 7.74 million combined SMSS/SAGES sample. Among these metal-deficient stars, we looked at 9,500 rapidly rotating stars with two methods to classify disk-like and halo-like candidates in the MW.

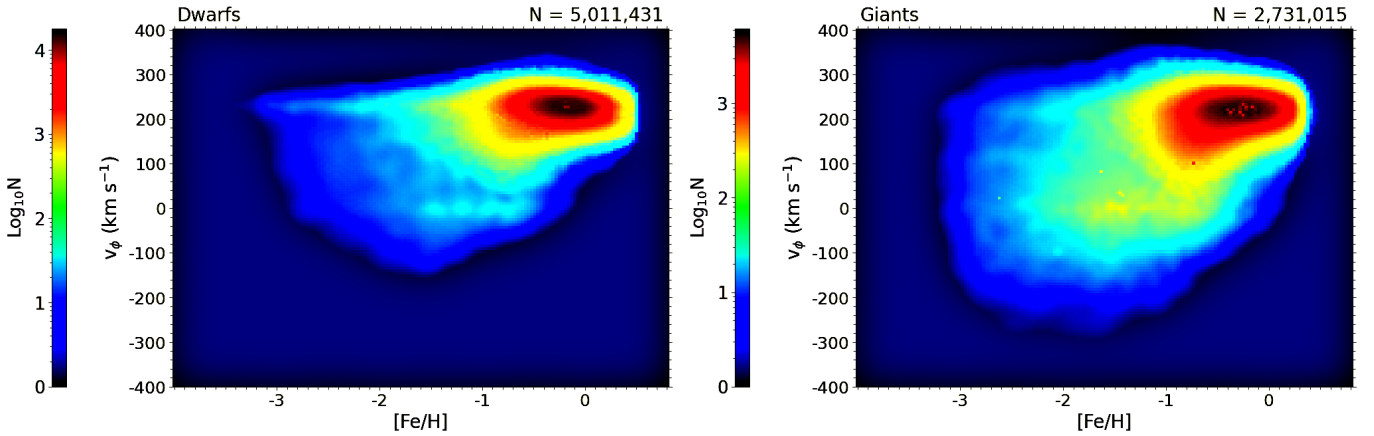
### 3.1. $v_\phi$ vs. [Fe/H]

Figure 3 shows plots of stellar number density for our sample in the rotational velocity vs. photometric-metallicity plane. In the left panel, the rapidly rotating disk system (comprising both the thin and thick disk) is most visible for  $[\text{Fe}/\text{H}] > -1$ . In addition, as reported in the series of papers by An & Beers (2020, 2021a,b), the MWTD, the Splashed Disk (SD), and a hint of the GSE substructure can be seen. However, the VMP/EMP stars in the rapidly rotating disk region ( $v_\phi > 150 \text{ km s}^{-1}$ ; the average value of rotational velocity for the MWTD from Carollo et al. 2010), are less visible than the other components. To make this feature more prominent, we applied an adaptive-kernel smoothing (ASMOOTH; Ebeling et al. 2006) procedure with the minimal number of pixels to be covered by the kernel (“PAR” parameter) set to 2.8, and an unsharp-masking procedure<sup>5</sup> to the

<sup>5</sup> The unsharp-masking procedure subtracts a blurred copy of the image and re-scales the image to obtain the same contrast of large (low-frequency) structures as in the input image. This is equivalent to adding a high-pass filtered image and thus sharpens the image. The “Radius (Sigma)” parameter is the standard deviation (blur radius) of the Gaussian blur that is subtracted. The “Mask Weight” parameter determines the strength of filtering, where “Mask Weight” = 1 would be an infinite weight of the high-pass filtered image that is added – see <https://imagej.nih.gov/ij/developer/api/ij/plugin/filter/UnsharpMask.html>.



**Figure 3.** Left panel: Rotational velocity distribution ( $v_\phi$ ) of our SMSS/SAGES sample as a function of photometric metallicity ( $[\text{Fe}/\text{H}]$ ). The number density is color-coded on a logarithmic scale. The total number of VMP/EMP stars is about 31,800. Right panel: Same as the left panel, but after applying the adaptive-kernel smoothing and unsharp-masking procedures (see text).



**Figure 4.** The  $v_\phi$  distribution as a function of  $[\text{Fe}/\text{H}]$ , for the dwarfs (left panel) and giants (right panel) in our SMSS/SAGES sample. The adaptive-kernel smoothing and unsharp-masking procedures are applied to both panels. There are about 8,400 VMP/EMP dwarfs and about 23,400 VMP/EMP giants.

density maps with “Radius (Sigma)” = 30 pixels and “Mask Weight” = 0.6, using the `Fiji` image processing package<sup>6</sup>, as shown in the right panel. The VMP/EMP disk system is now more evident.

### 3.2. Dwarfs and Giants

Figure 4 presents number-density plots in the rotational velocity vs. photometric metallicity plane (with the adaptive-kernel smoothing and unsharp-masking procedures applied) for dwarfs (left panel) and giants (right panel) in the SMSS/SAGES data set. There are about 8,400 VMP/EMP dwarfs, and 23,400 VMP/EMP giants. The subsets of these stars with  $v_\phi > 150 \text{ km s}^{-1}$  number 4,070 VMP/EMP dwarfs and 5,400 VMP/EMP giants.

<sup>6</sup> <https://imagej.net/software/fiji/>

### 3.3. Fractions of Disk-like and Halo-like Stars

#### 3.3.1. Based on the $Z_{\text{max}}$ Criterion

We first consider metal-poor (MP;  $[\text{Fe}/\text{H}] \leq -1$ ) stars in three regions of  $Z_{\text{max}}$ :  $Z_{\text{max}} > 3 \text{ kpc}$ ,  $Z_{\text{max}} \leq 3 \text{ kpc}$ , and  $Z_{\text{max}} \leq 1 \text{ kpc}$ . We assign the stars with  $Z_{\text{max}} > 3 \text{ kpc}$  to the halo populations, while those with  $Z_{\text{max}} \leq 3 \text{ kpc}$  and  $Z_{\text{max}} \leq 1 \text{ kpc}$  are candidate members of the metal-poor thick- and thin-disk systems, respectively. The left panel of Figure 5 shows the cumulative numbers of each population. At  $[\text{Fe}/\text{H}] \leq -2$ , approximately 24,300 halo stars with  $Z_{\text{max}} > 3 \text{ kpc}$  were found, along with about 13,050 stars with  $Z_{\text{max}} \leq 3 \text{ kpc}$  and 4,200 stars with  $Z_{\text{max}} \leq 1 \text{ kpc}$ . The middle panel shows the cumulative distribution function (CDF) for each population, normalized by the number of MP stars. Roughly 18.2% of the MP stars assigned to the halo system are VMP stars and 0.46% are EMP stars; about 7.5% of the MP stars assigned to the disk system are VMP stars, and 0.33% are

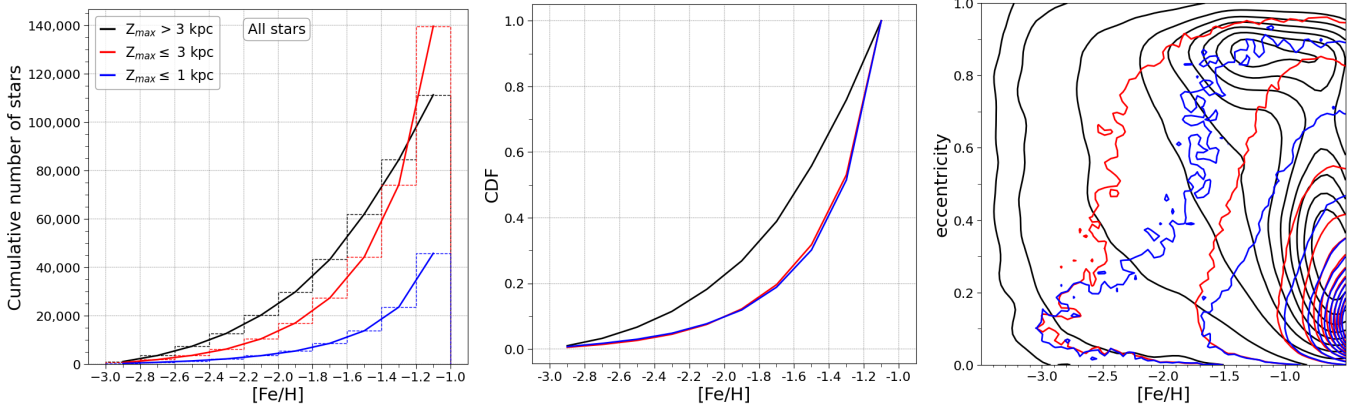


**Figure 5.** Left panel: Cumulative number distribution of the MP ( $[\text{Fe}/\text{H}] \leq -1$ ) stars as a function of  $[\text{Fe}/\text{H}]$ , for stars with  $Z_{\text{max}} > 3$  kpc (black line),  $Z_{\text{max}} \leq 3$  kpc (red line), and  $Z_{\text{max}} \leq 1$  kpc (blue line). Middle panel: Cumulative distribution functions of  $[\text{Fe}/\text{H}]$  for these subsamples. Each population is normalized on the basis of the number of stars at  $[\text{Fe}/\text{H}] = -1$ . Right panel: Contour map of the eccentricity distribution as a function of  $[\text{Fe}/\text{H}]$  for the same subsamples. Contour lines represent 15, 25, 35, 45, 55, 65, 75, 85, 95, 99.5, and 99.95 percent of the cumulative distribution of each sample.

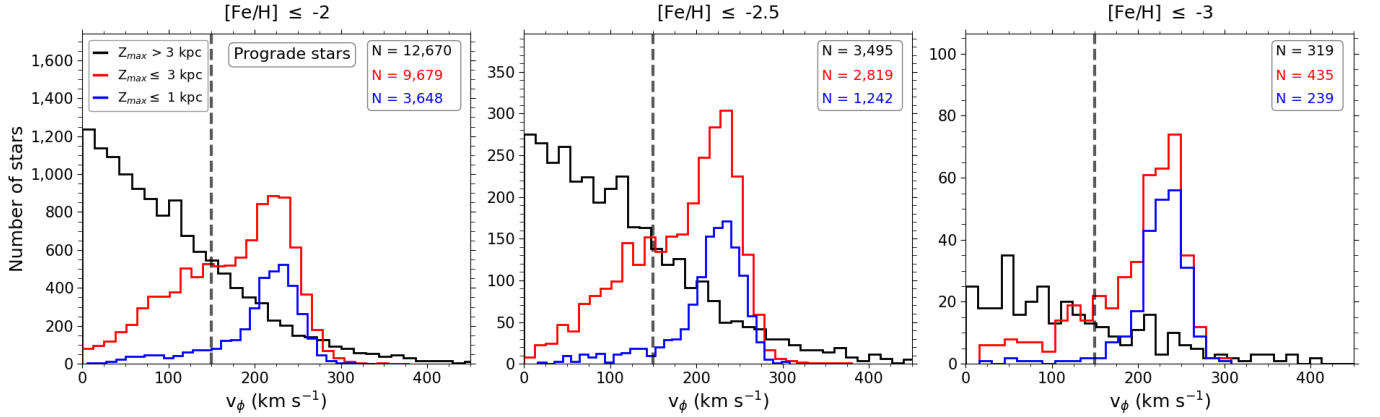


**Figure 6.** Number distributions of VMP/EMP stars with prograde orbits as a function of rotational velocity ( $v_\phi$ ). The vertical dashed line is at  $v_\phi = 150 \text{ km s}^{-1}$ , which is used to select disk-like stars on highly prograde orbits.

EMP stars. It is also interesting to note that the CDFs of the stars with  $Z_{\text{max}} \leq 3$  kpc and  $Z_{\text{max}} \leq 1$  kpc are essentially identical.

The right panel of Figure 5 is a contour map of orbital eccentricity for these subsamples split on  $Z_{\text{max}}$ . The broad distribution of eccentricity, peaking at high eccentricity, for stars kinematically assigned to the halo population is clear, as is the presence of low-eccentricity stars among the stars assigned to the disk system. Note at this point we have not applied any cuts on  $v_\phi$ , only on  $Z_{\text{max}}$ , so we expect that the subsamples of stars with  $Z_{\text{max}} \leq 3$  kpc and  $Z_{\text{max}} \leq 1$  kpc have some level of contamination from halo stars.

Figure 6 shows the distribution of  $v_\phi$  for these three subsamples, but only for stars with  $[\text{Fe}/\text{H}] \leq -2$ ,  $[\text{Fe}/\text{H}] \leq -2.5$ , and  $[\text{Fe}/\text{H}] \leq -3$ , from the left to right panels, respectively. The vertical dashed line corresponds to a cut on  $v_\phi = 150 \text{ km s}^{-1}$ , the average orbital rotation value for the MWTD from [Carollo et al. \(2010\)](#). We note that the adopted

limit for the MWTD stars with the lowest  $v_\phi$  from [Carollo et al.](#) (as well as from [An & Beers 2021b](#)) is  $v_\phi \sim 100 \text{ km s}^{-1}$ . From inspection, there remains considerable contamination of the VMP/EMP stars with prograde disk-like orbits by stars with prograde halo-like orbits, even with the higher cut at  $v_\phi > 150 \text{ km s}^{-1}$  (although it is substantially less for the EMP stars shown in the right-hand panel), indicating that a more sophisticated separation methodology is desirable.

Figure 7 shows histograms of the eccentricity distribution for stars with  $[\text{Fe}/\text{H}] \leq -2$ ,  $[\text{Fe}/\text{H}] \leq -2.5$ , and  $[\text{Fe}/\text{H}] \leq -3$ , respectively. We now subdivide the stars into three regions:  $Z_{\text{max}} > 3$  kpc,  $1 < Z_{\text{max}} \leq 3$  kpc, and  $Z_{\text{max}} \leq 1$  kpc, in an attempt to better isolate stars with thick-disk orbits from those with thin-disk orbits. We note that these divisions are imperfect, in that we expect there to be contamination from halo stars at all  $Z_{\text{max}}$ . Within the  $1 < Z_{\text{max}} \leq 3$  kpc region there should be few thin-disk stars. Within the cut  $Z_{\text{max}} \leq 1$  kpc there will also remain some contamination from thick-disk stars.

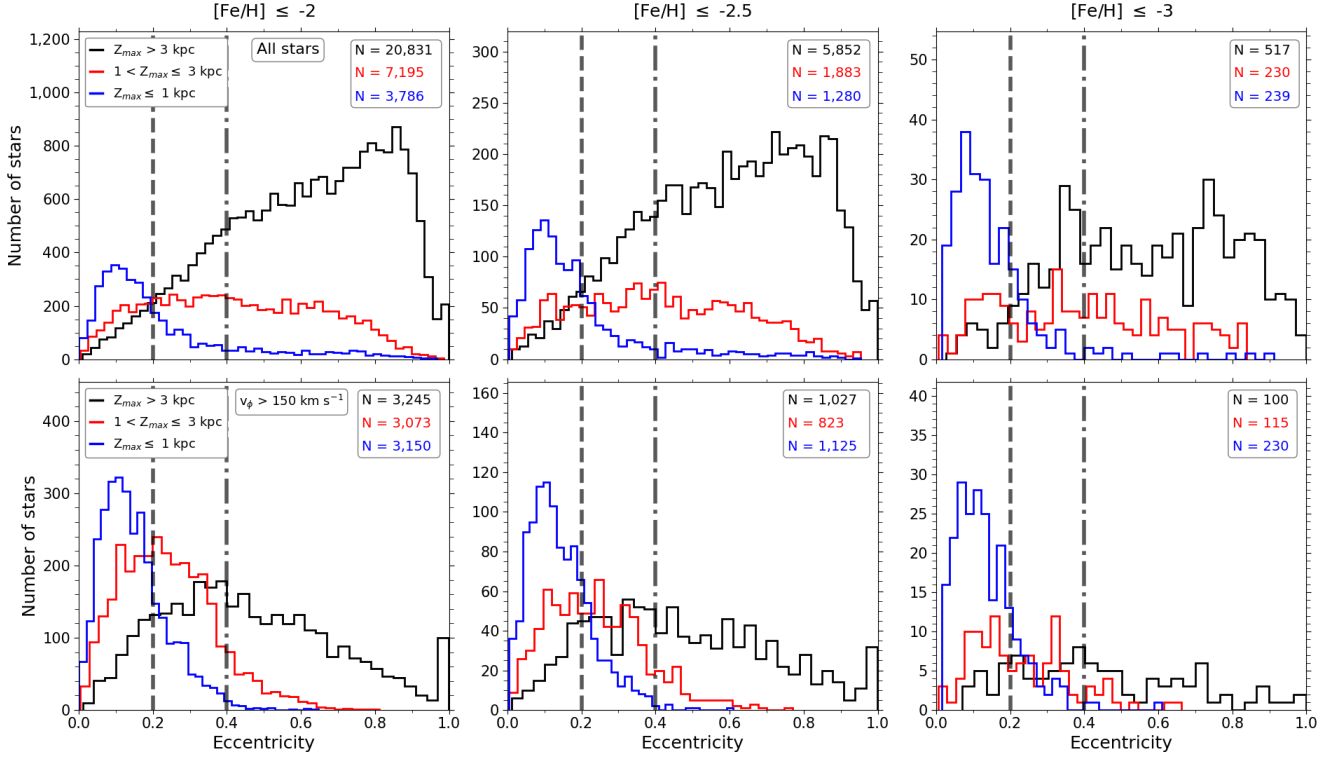


**Figure 7.** Top panels: Number distributions of VMP/EMP stars on both retrograde and prograde orbits as a function of eccentricity, from the left to the right panel, for  $[\text{Fe}/\text{H}] \leq -2$ ,  $\leq -2.5$ , and  $\leq -3$ , respectively. The black, red, and blue solid lines indicate the stars with  $Z_{\text{max}} > 3$  kpc,  $1 < Z_{\text{max}} \leq 3$  kpc, and  $Z_{\text{max}} \leq 1$  kpc. The number of stars in each region is indicated in the legend on the top right of the panels. The dashed and dot-dashed lines are shown at eccentricity = 0.2 and 0.4. Bottom panels: Same as top panels, but for the highly prograde stars with  $v_{\phi} > 150 \text{ km s}^{-1}$ .

From inspection of the upper row of panels, which includes stars on both retrograde and prograde orbits, the VMP/EMP stars with disk-like, very low-eccentricity orbits ( $\text{ecc} \leq 0.2$ ) dominate over those with higher-eccentricity orbits in all three ranges of  $[\text{Fe}/\text{H}]$ , with the relative proportions increasing with decreasing metallicity. In the bottom row of panels, the introduction of the  $v_{\phi} > 150 \text{ km s}^{-1}$  cut greatly increases the relative dominance of VMP/EMP stars with disk-like orbits, including for stars with  $\text{ecc} \leq 0.4$ .

### 3.3.2. Based on the Haywood Criterion

There is also evidence for the existence of a VMP/EMP disk system from the Haywood Diagram. Figure 8 shows the distribution of the arctangent of the  $Z_{\text{max}}/R_{\text{max}}$  values (defined here as the inclination angle,  $IA$ ) for VMP/EMP stars, following Haywood et al. (2018) and Di Matteo et al. (2020). The panels show this distribution for stars with the total numbers of VMP/EMP stars (black line), for stars with prograde orbits (purple line), and with retrograde orbits (orange line), respectively, for stars in the regions with  $[\text{Fe}/\text{H}] \leq -2$ ,  $\leq -2.5$ , and  $\leq -3$ . The vertical dashed line and dot-dashed line show the approximate “troughs” in the distributions at  $IA = 0.25$  and  $0.65$  radians, respectively, which can be used to roughly separate likely halo stars, thick-disk stars,

and thin-disk stars. The numbers shown in each region listed in the figure reveal that VMP/EMP stars with prograde orbits dominate over those with retrograde orbits for  $IA \leq 0.25$  radians and those with  $0.25 < IA \leq 0.65$  radians, and much less so for  $IA > 0.65$  radians. One can reasonably associate the prograde stars with  $IA \leq 0.25$  radians with thin-disk orbits, those with  $0.25 < IA \leq 0.65$  radians with thick-disk orbits, and those with  $IA > 0.65$  radians with halo-like orbits.

If we now specialize to the highly prograde stars with orbital velocities  $v_{\phi} > 150 \text{ km s}^{-1}$  (indicated by the blue-shaded region in Figure 8), the relative dominance of the stars in the disk-like system for VMP/EMP stars becomes even more clear.

Figure 9 is a plot of  $Z_{\text{max}}$  vs.  $R_{\text{max}}$  for the stars with  $[\text{Fe}/\text{H}] \leq -2$ ,  $\leq -2.5$ , and  $\leq -3$ , in the left, middle, and right panels, respectively. The upper panels of this figure show plots of the  $Z_{\text{max}}$  distribution as a function of  $R_{\text{max}}$  for the full sample of prograde stars ( $v_{\phi} > 0 \text{ km s}^{-1}$ ). The dashed and dot-dashed lines corresponding to the troughs shown in Figure 8 at  $IA = 0.25$  and  $0.65$  radians, respectively. The number of stars is provided in the legend at the top of each panel. The bottom panels apply to the stars on highly prograde orbits ( $v_{\phi} > 150 \text{ km s}^{-1}$ ). From inspection, the



separation of the regions becomes much more pronounced when the highly prograde stars are considered.

Figure 10 shows histograms of the eccentricity distribution for stars with  $[\text{Fe}/\text{H}] \leq -2$ ,  $\leq -2.5$ , and  $\leq -3$ , respectively. The colors represent the same cuts on  $IA$  as in Figure 8. From inspection of the upper row of panels, which includes stars on both retrograde and prograde orbits, the VMP/EMP stars with disk-like, very low-eccentricity orbits ( $\text{ecc} < 0.2$ ) dominate over those with higher-eccentricity orbits in all three ranges of  $[\text{Fe}/\text{H}]$ , with the relative proportions increasing with decreasing metallicity. In the bottom row of panels, the introduction of the  $v_\phi > 150 \text{ km s}^{-1}$  cut greatly increases the relative dominance of VMP/EMP stars with disk-like orbits, including for stars with  $\text{ecc} \leq 0.4$ .

In summary, a total of 8,037 candidate VMP/EMP stars with  $v_\phi > 150 \text{ km s}^{-1}$  were identified, considering the 6,185 stars among the 6,223 and 7,999 disk-like candidates from the  $Z_{\text{max}}$  and Haywood criteria that were selected by both methods.

#### 4. DISCUSSION

In the recent literature, increasing attention has been drawn to the existence of VMP/EMP stars that appear to be members of the MW disk system, based on a variety of samples and using a number of different techniques in order to approximately separate such stars from those that are likely to be members of the halo system. Separation based on the  $Z_{\text{max}}$  criterion, although capable of identifying a relatively pure sample of stars with halo-like orbits, has considerable potential contamination of stars with disk-like orbits by halo-like stars. The Haywood criterion, based on the separation of stars in different dynamical populations, produces a more pure sample of stars with thick-disk and thin-disk orbits, especially when eccentricity is considered in conjunction.

As we have demonstrated in this paper, the large numbers of stars now available with photometric-metallicity estimates from SMSS and SAGES have increased the numbers of candidate disk-system VMP/EMP stars dramatically.

We refer to these stars as candidates for two reasons. First, the metallicity estimates, though of similar accuracy to those obtained from low- to medium-resolution spectroscopy, may be influenced by the presence of strong molecular CN bands, in particular for the most metal-poor stars. We have taken steps to mitigate this behavior, as described in the Appendix. They should be confirmed by follow-up spectroscopy. Secondly, the question remains whether at least some of the apparent disk-system VMP/EMP stars represent members of an early forming *in-situ* primordial disk system, prior to additional stars being added from accreted dwarf satellites, or are possibly a very/extremely low-metallicity tail of the long-recognized MWTD component of the MW. These alternatives may prove difficult to differentiate between based on

kinematics alone, as mergers with dwarf galaxies could readily perturb the orbits of stars that were born in a primordial thin- or thick-disk.

The best way to distinguish between these two possibilities may be to conduct a thorough study of their elemental abundances, and look for differences as a function of declining metallicity. Feltzing & Feuillet (2023) have recently used elemental-abundance information from APOGEE, in combination with kinematics, in order to identify the likely presence of an early disk structure in the inner disk of the MW including VMP stars (although they are limited by the lack of lower-metallicity stars in APOGEE to verifying that EMP stars are present as well). Detailed chemical abundances for our candidate VMP/EMP stars will clearly be useful.

Additional information should soon be available from the J-PLUS and S-PLUS photometric surveys, which can obtain estimates for C and Mg (as well as N and Ca, once ongoing calibrations are completed), in addition to  $[\text{Fe}/\text{H}]$ , thanks to their narrow/medium band-pass filters. More complete information will require high-resolution spectroscopic follow-up for at least a subset of the VMP/EMP candidates. Determination of more accurate age estimates than we have at present for candidate VMP/EMP stars on disk-like orbits may also prove illuminating.

Beyond the identification of the VMP/EMP disk-system candidates, we can speculate on their origins by considering numerical simulations of MW-like galaxies. We analyzed the data from a high-resolution cosmological zoom-in simulation of a Milky Way-like galaxy with a halo mass of  $1.2 \times 10^{12} M_\odot$  presented in Hirai et al. (2022). These authors defined the *in-situ* component as stars formed in the main halo of the central galaxy, whereas the accreted component were defined as stars coming from dwarf galaxy satellites. Data within the Galactocentric distance  $r_{\text{GC}}$  between 3 to 20 kpc were taken; this region roughly corresponds to the observed area by SMSS and SAGES.

From this simulation, we found that 8% and 92% of stars with  $v_\phi > 150 \text{ km s}^{-1}$  and  $[\text{Fe}/\text{H}] \leq -2$  are formed in the *in-situ* and accreted components, respectively. We also found that 96% of VMP/EMP stars with  $v_\phi > 150 \text{ km s}^{-1}$  have ages  $> 10 \text{ Gyr}$ .

Similar results have been shown in the analysis of IllustrisTNG50 simulations by Mardini et al. (2022a) and Carollo et al. (2023). Most recently, Sotillo-Ramos et al. (2023) considered a large sample of 138 MW analogs from the TNG50 cosmological simulations, and found that, across all of these analogs, about 20% of the VMP/EMP stars have disk-like orbits, with some analogs reaching as high as 30%. Roughly half of their disk-like stars have average ages exceeding 12.5 Gyr, with 70% coming from accreted dwarf galaxies. Taken as a whole, the simulation results suggest that VMP/EMP stars with disk-like orbits comprise stars

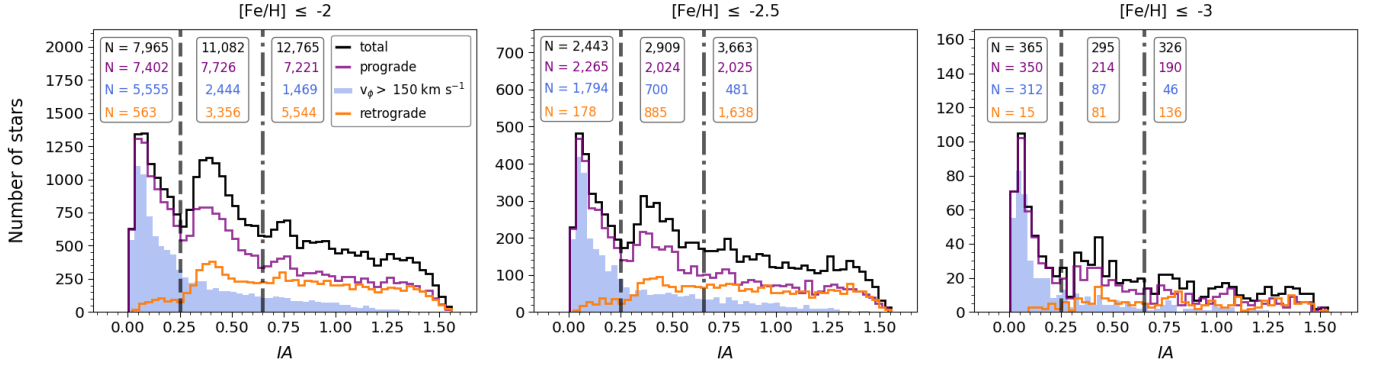


**Figure 8.** Number distribution of VMP/EMP stars as a function of  $IA$ , for  $[Fe/H] \leq -2$ ,  $\leq -2.5$ , and  $\leq -3$ , from the left to the right panel, respectively. The total, prograde, and retrograde orbiting stars are in black, purple, and orange lines, respectively. The prograde stars with  $v_\phi > 150 \text{ km s}^{-1}$  are shaded in blue. The number of stars in each region is indicated in the legend on the top of the panels. The dashed and dot-dashed lines indicate  $IA = 0.25$  and  $0.65$  radians.

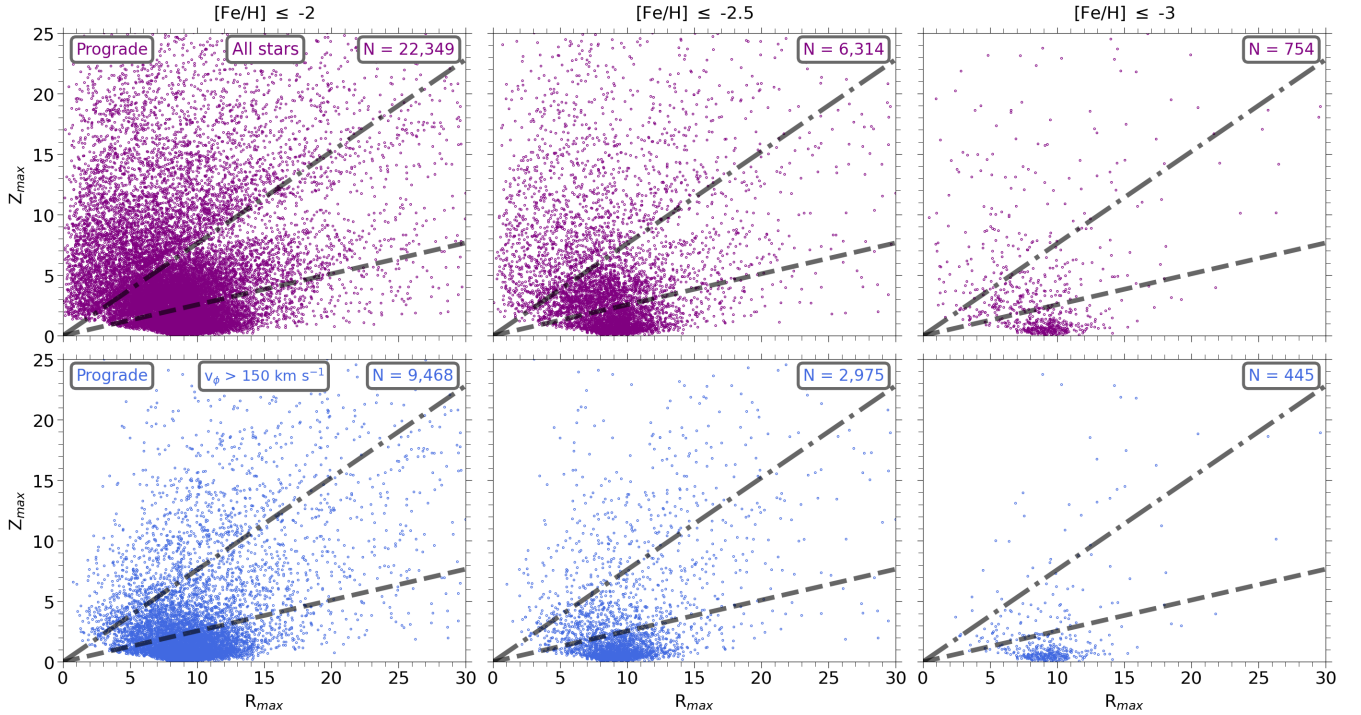


**Figure 9.** Top panels: The  $Z_{\max}$  distribution as a function of  $R_{\max}$  for the full sample of prograde stars. The dashed and dot-dashed lines at  $IA = 0.25$  and  $0.65$  radians are shown. The number of stars is shown in the legend at the top right of each panel. Bottom panels: Same as in the top panels, but for the stars with  $v_\phi > 150 \text{ km s}^{-1}$ .

coming primarily from accreted dwarf galaxies and *in-situ* stars formed in an early primordial disk, or are associated with the MWTD.

Fractions of stars with prograde orbits can also inform the origin of VMP/EMP stars. Figure 11 compares the prograde fractions as a function of  $[Fe/H]$  for our sample and the simulation of Hira et al. (2022). For  $[Fe/H] > -2.0$ , both our SMSS/SAGES sample and the simulation show an increasing trend toward higher metallicity, attributable to disk formation. On the other hand, the prograde fraction in our sample is roughly constant as a function of  $[Fe/H]$  for VMP/EMP

stars. In the lowest-metallicity regime, the fraction rises to 0.76, reflecting the higher fraction of disk-like orbits among EMP stars (Figures 7 and 10). This tendency is not clearly seen in the simulation. However, note that our sample's prograde fraction for VMP/EMP stars is significantly larger than that of the simulation. It should be kept in mind that the Hira et al. (2022) simulation is for a single realization, when in fact a variety of galaxy-assembly histories are likely to have different outcomes, as demonstrated by other recent simulation studies (e.g., Santistevan et al. 2021).

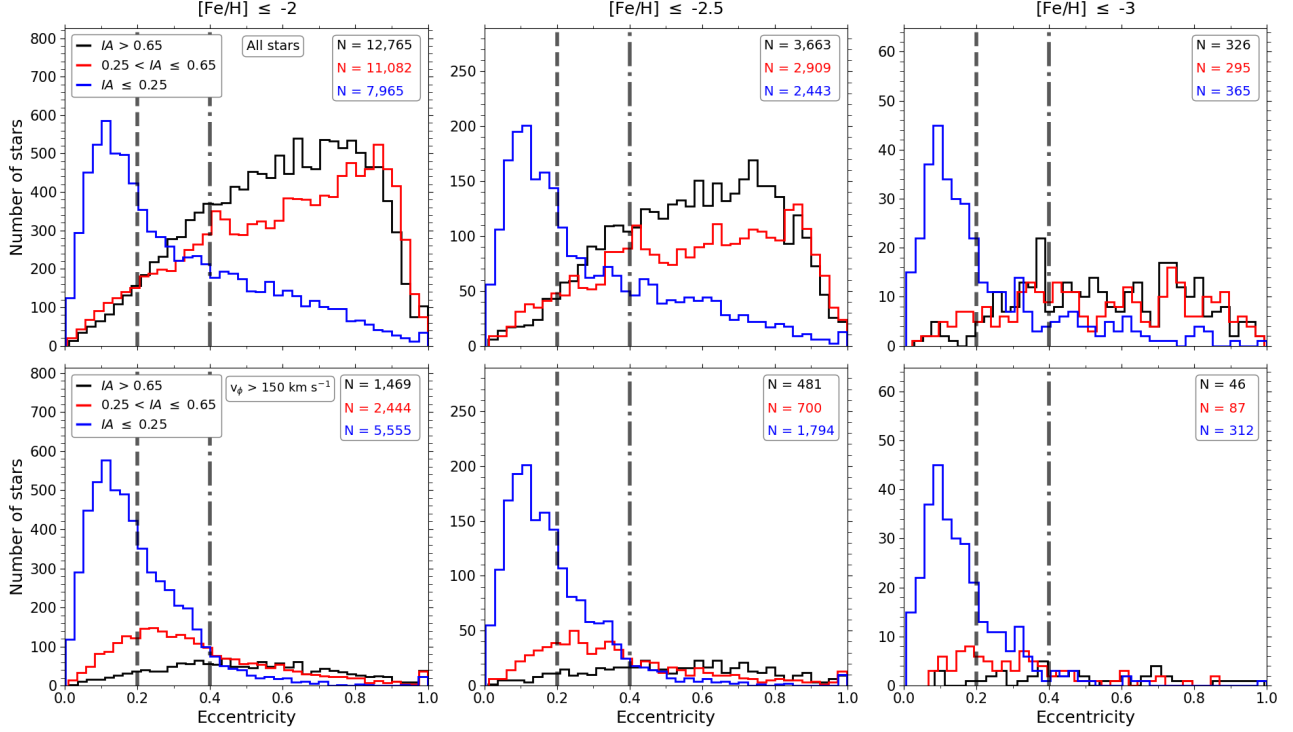


**Figure 10.** Top panels: Number distributions of VMP/EMP stars as a function of eccentricity, from the left to the right panel, for  $[\text{Fe}/\text{H}] \leq -2$ ,  $\leq -2.5$ , and  $\leq -3$ , respectively. The black, red, and blue solid lines indicate the stars with  $IA > 0.65$ ,  $0.25 < IA \leq 0.65$ , and  $IA \leq 0.25$  radians, respectively. The dashed and dot-dashed lines are shown at eccentricity = 0.2 and 0.4. The number of stars in each region is indicated in the legend at the top right of the panels. Bottom panels: Same as in the top panels, but for the highly prograde stars with  $v_\phi > 150 \text{ km s}^{-1}$ .

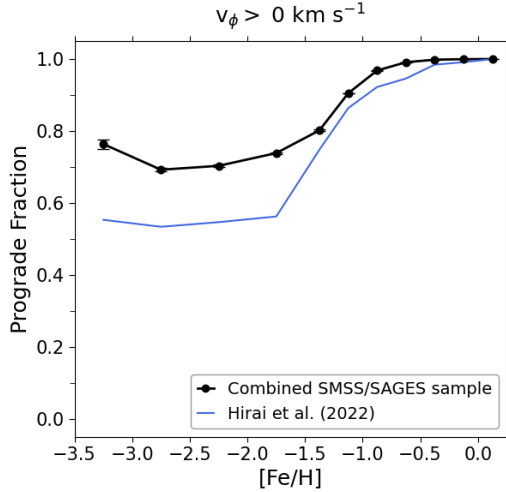


**Figure 11.** Fraction of prograde stars as a function of  $[\text{Fe}/\text{H}]$ . The black line shows the combined SMSS/SAGES sample. The blue line is the simulation results of Hirai et al. (2022) and the Galactocentric distance of the data is confined between 3 to 20 kpc, roughly corresponding to the combined SMSS/SAGES sample. The error bars shown are calculated using the normal approximation for the binomial proportions. Due to the large number of stars included in our data set, they are quite small.

Prograde orbit fractions higher than 0.5 for  $[\text{Fe}/\text{H}] < -2$  suggest the accretion of satellites preferentially on prograde

orbits or early disk formation at low metallicity. Carter et al. (2021) also reported a high prograde fraction, between 0.7 and 0.8, but with significantly larger error bars due to the smaller sample they considered (see the upper left panel of their Figure 3). They have also shown that the prograde fraction converges to 0.5 with a model assuming an isotropic distribution of orbits in the stellar halo (Rybizki et al. 2018). We confirm their results with a larger sample. Recently, Li et al. (2022b) have shown that 10 out of 12 MW stellar streams with an average  $[\text{Fe}/\text{H}] \approx -2$  are on prograde orbits. These enhanced prograde fractions mean that the MW’s VMP/EMP stars tend to be formed in accreted components with prograde orbits or in an ancient disk. As discussed above, spectroscopic follow-up of our candidate disk-like VMP/EMP stars may help improve estimates of the relative fractions associated with these differing origins.

For convenience of future comparisons of our observations with those of others, and with numerical simulations, Table 1 provides a summary of the numbers, fractions, and orbital characteristics of the SMSS/SAGES sample for different cuts on  $[\text{Fe}/\text{H}]$ ,  $Z_{\text{max}}$ , and  $IA$ . Note that, with the exception of the first line in each subsection of the table (indicated as “All”) the fractions refer to the total numbers of stars listed on the first line at the top of each column in the subsection.

**Table 1.** Numbers, Fractions, and Orbital Characteristics of MP/VMP/EMP Stars in the SMSS/SAGES Sample

Full Sample of MP Stars				
	$[\text{Fe}/\text{H}] \leq -1$	$[\text{Fe}/\text{H}] \leq -2$	$[\text{Fe}/\text{H}] \leq -2.5$	$[\text{Fe}/\text{H}] \leq -3$
<b>All</b> ( $N_{\text{tot}} = 251,908$ )	<b>251,908 (100.0 %)</b>	<b>31,812 (12.6 %)</b>	<b>9,015 (3.6 %)</b>	<b>986 (0.4 %)</b>
Prograde	206,376 (81.9 %)	22,349 (70.3 %)	6,314 (70.0 %)	754 (76.5 %)
Retrograde	45,532 (18.1 %)	9,463 (29.7 %)	2,701 (30.0 %)	232 (23.5 %)
Dwarf	80,996 (32.2 %)	8,443 (26.5 %)	2,550 (28.3 %)	342 (34.7 %)
Giant	170,912 (67.8 %)	23,369 (73.5 %)	6,465 (71.7 %)	644 (65.3 %)
	$-1 \geq [\text{Fe}/\text{H}] > -2$	$-2 \geq [\text{Fe}/\text{H}] > -2.5$	$-2.5 \geq [\text{Fe}/\text{H}] > -3$	$[\text{Fe}/\text{H}] \leq -3$
<b>All</b> ( $N_{\text{tot}} = 251,908$ )	<b>220,096 (87.4 %)</b>	<b>22,797 (9.0 %)</b>	<b>8,029 (3.2 %)</b>	<b>986 (0.4 %)</b>
Prograde	184,027 (83.6 %)	16,035 (70.3 %)	5,560 (69.2 %)	754 (76.5 %)
Retrograde	36,069 (16.4 %)	6,762 (29.7 %)	2,469 (30.8 %)	232 (23.5 %)
Dwarf	72,553 (33.0 %)	5,893 (25.8 %)	2,208 (27.5 %)	342 (34.7 %)
Giant	147,543 (67.0 %)	16,904 (74.2 %)	5,821 (72.5 %)	644 (65.3 %)
$Z_{\text{max}}$ Criterion Separation of Orbits for VMP/EMP Stars				
$[\text{Fe}/\text{H}] \leq -2$	$Z_{\text{max}} > 3 \text{ kpc}$	$Z_{\text{max}} \leq 3 \text{ kpc}$	$1 \text{ kpc} < Z_{\text{max}} \leq 3 \text{ kpc}$	$Z_{\text{max}} \leq 1 \text{ kpc}$
<b>All</b> ( $N_{\text{tot}} = 31,812$ )	<b>20,831 (65.5 %)</b>	<b>10,981 (34.5 %)</b>	<b>7,195 (22.6 %)</b>	<b>3,786 (11.9 %)</b>
Prograde	12,670 (60.8 %)	9,679 (88.1 %)	6,031 (83.8 %)	3,648 (96.4 %)
Retrograde	8,161 (39.2 %)	1,302 (11.9 %)	1,164 (16.2 %)	138 (3.6 %)
Highly prograde	3,245 (15.6 %)	6,223 (56.7 %)	3,073 (42.7 %)	3,150 (83.2 %)
Highly prograde, $\text{ecc} \leq 0.4$	1,474 (7.1 %)	5,860 (53.4 %)	2,743 (38.1 %)	3,117 (82.3 %)
Highly prograde, $\text{ecc} \leq 0.2$	438 (4.0 %)	3,668 (33.4 %)	1,266 (17.6 %)	2,402 (63.4 %)
$[\text{Fe}/\text{H}] \leq -2.5$	$Z_{\text{max}} > 3 \text{ kpc}$	$Z_{\text{max}} \leq 3 \text{ kpc}$	$1 \text{ kpc} < Z_{\text{max}} \leq 3 \text{ kpc}$	$Z_{\text{max}} \leq 1 \text{ kpc}$
<b>All</b> ( $N_{\text{tot}} = 9,015$ )	<b>5,852 (64.9 %)</b>	<b>3,163 (35.1 %)</b>	<b>1,883 (20.9 %)</b>	<b>1,280 (14.2 %)</b>
Prograde	3,495 (59.7 %)	2,819 (89.1 %)	1,577 (83.7 %)	1,242 (97.0 %)
Retrograde	2,357 (40.3 %)	344 (10.9 %)	306 (16.3 %)	38 (3.0 %)
Highly Prograde	1,027 (17.5 %)	1,948 (61.6 %)	823 (43.7 %)	1,125 (87.9 %)
Highly prograde, $\text{ecc} \leq 0.4$	452 (7.7 %)	1,846 (58.4 %)	728 (38.7 %)	1,118 (87.3 %)
Highly prograde, $\text{ecc} \leq 0.2$	141 (2.4 %)	1,237 (39.1 %)	350 (18.6 %)	887 (69.3 %)
$[\text{Fe}/\text{H}] \leq -3$	$Z_{\text{max}} > 3 \text{ kpc}$	$Z_{\text{max}} \leq 3 \text{ kpc}$	$1 \text{ kpc} < Z_{\text{max}} \leq 3 \text{ kpc}$	$Z_{\text{max}} \leq 1 \text{ kpc}$
<b>All</b> ( $N_{\text{tot}} = 986$ )	<b>517 (52.4 %)</b>	<b>69 (47.6 %)</b>	<b>230 (23.3 %)</b>	<b>239 (24.2 %)</b>
Prograde	319 (61.7 %)	435 (92.8 %)	196 (85.2 %)	239 (100.0 %)
Retrograde	198 (38.3 %)	34 (7.2 %)	34 (14.8 %)	0 (0.0 %)
Highly Prograde	100 (19.3 %)	345 (73.6 %)	115 (50.0 %)	230 (96.2 %)
Highly prograde, $\text{ecc} \leq 0.4$	50 (9.7 %)	329 (70.1 %)	102 (44.3 %)	227 (95.0 %)
Highly prograde, $\text{ecc} \leq 0.2$	16 (3.1 %)	248 (52.9 %)	57 (24.8 %)	191 (79.9 %)



Haywood Criterion Separation of Orbits for VMP/EMP Stars				
$[\text{Fe}/\text{H}] \leq -2$	$IA > 0.65$	$IA \leq 0.65$	$0.25 < IA \leq 0.65$	$IA \leq 0.25$
<b>All (<math>N_{\text{tot}} = 31,812</math>)</b>	<b>12,765 (40.1 %)</b>	<b>19,047 (59.9 %)</b>	<b>11,082 (34.8 %)</b>	<b>7,965 (25.0 %)</b>
Prograde	7,221 (56.6 %)	15,128 (79.4 %)	7,726 (69.7 %)	7,402 (92.9 %)
Retrograde	5,544 (43.4 %)	3,919 (20.6 %)	3,356 (30.3 %)	563 (7.1 %)
Highly Prograde	1,469 (11.5 %)	7,999 (42.0 %)	2,444 (22.1 %)	5,555 (69.7 %)
Highly prograde, $\text{ecc} \leq 0.4$	543 (4.3 %)	6,791 (35.7 %)	2,125 (19.2 %)	5,173 (64.9 %)
Highly prograde, $\text{ecc} \leq 0.2$	147 (1.2 %)	3,959 (20.8 %)	633 (5.7 %)	3,368 (42.3 %)
$[\text{Fe}/\text{H}] \leq -2.5$	$IA > 0.65$	$IA \leq 0.65$	$0.25 < IA \leq 0.65$	$IA \leq 0.25$
<b>All (<math>N_{\text{tot}} = 9,015</math>)</b>	<b>3,663 (40.6 %)</b>	<b>5,352 (59.4 %)</b>	<b>2,909 (32.3 %)</b>	<b>2,443 (27.1 %)</b>
Prograde	2,025 (55.3 %)	4,289 (80.1 %)	2,024 (69.6 %)	2,265 (92.7 %)
Retrograde	1,638 (44.7 %)	1,063 (19.9 %)	885 (30.4 %)	178 (7.3 %)
Highly prograde	481 (13.1 %)	2,494 (46.6 %)	700 (24.1 %)	1,794 (73.4 %)
Highly prograde, $\text{ecc} \leq 0.4$	156 (4.3 %)	2,142 (40.0 %)	619 (21.3 %)	1,676 (68.6 %)
Highly prograde, $\text{ecc} \leq 0.2$	43 (1.2 %)	1,335 (24.9 %)	184 (6.3 %)	1,161 (47.5 %)
$[\text{Fe}/\text{H}] \leq -3$	$IA > 0.65$	$IA \leq 0.65$	$0.25 < IA \leq 0.65$	$IA \leq 0.25$
<b>All (<math>N_{\text{tot}} = 986</math>)</b>	<b>326 (33.1 %)</b>	<b>660 (66.9 %)</b>	<b>295 (29.9 %)</b>	<b>365 (37.0 %)</b>
Prograde	190 (58.3 %)	564 (85.5 %)	214 (72.5 %)	350 (95.9 %)
Retrograde	136 (41.7 %)	96 (14.5 %)	81 (27.5 %)	15 (4.1 %)
Highly prograde	46 (14.1 %)	399 (60.5 %)	87 (29.5 %)	312 (85.5 %)
Highly prograde, $\text{ecc} \leq 0.4$	18 (5.5 %)	361 (54.7 %)	84 (28.5 %)	296 (81.1 %)
Highly prograde, $\text{ecc} \leq 0.2$	4 (1.2 %)	260 (39.4 %)	30 (10.2 %)	231 (63.3 %)

## 5. SUMMARY AND FUTURE PROSPECTS

We have identified over 8,000 candidate VMP/EMP disk-system stars in the MW from a subset of the  $\sim 50$  million stars from SMSS and SAGES with available photometric-metallicity estimates, based on calibrated  $u - G_{\text{BP}}$  colors and  $v - G_{\text{BP}}$  colors, a combination of the  $u/v$ -bands from SMSS/SAGES and the ultra wide-band *Gaia*  $G_{\text{BP}}$  prism spectra (Huang et al. 2022, 2023). We then trimmed the combined sample, eliminating photometrically identified binaries, cool dwarfs, and likely members of globular clusters. We then obtain the subset of 11.5 million stars in the combined sample with available RVs, proper motions, and distance estimates.

After the determination of dynamical parameters, we remove likely unbound stars, and excise stars with errors in their orbital rotation velocities  $v_\phi > 25 \text{ km s}^{-1}$  and relative

errors in  $Z_{\text{max}}$  (maximum orbital distance from the Galactic plane) and in  $R_{\text{max}}$  (maximum orbital apocentric distance projected on to the plane)  $\geq 30\%$ , leaving a total sample of about 7.74 million stars.

We then apply two methods to separate stars with halo-like and disk-like orbits. The first approach considered stars with  $Z_{\text{max}} > 3 \text{ kpc}$  to have halo-like orbits, and those with  $Z_{\text{max}} \leq 3 \text{ kpc}$  to have disk-like orbits. Our analysis indicates there exists a significant population of candidate VMP/EMP disk-system stars, moving on rapid prograde orbits ( $v_\phi > 150 \text{ km s}^{-1}$ ), increasing their relative populations with declining metallicity. We also split the stars with disk-like orbits into the regions  $1 < Z_{\text{max}} \leq 3 \text{ kpc}$ , and  $Z_{\text{max}} \leq 1 \text{ kpc}$ , in an attempt to better isolate stars with thick-disk orbits from those with thin-disk orbits. Based on this criterion, we find that 62% of the VMP stars have highly prograde disk-like or-

bits (2,958 stars on thick-disk orbits, 2,920 stars on thin-disk orbits), while 74% of the EMP stars have highly prograde disk-like orbits (115 stars on thick-disk orbits, 230 stars on thin-disk orbits). These fractions increase further if one also takes the eccentricity of the orbits into account.

The second approach considered the stars populating wedges in the diagram of  $Z_{\max}$  vs.  $IA$ , which redistributes corresponding to different dynamical populations of stars with halo-like and disk-like orbits. Our analysis indicates there exists a significant population of candidate VMP/EMP disk-system stars moving on rapid prograde orbits ( $v_\phi > 150 \text{ km s}^{-1}$ ), increasing their relative populations with declining metallicity. Based on the Haywood criterion, we find that 41% of the VMP stars have highly prograde disk-like orbits (2,357 stars on thick-disk orbits, 5,243 stars on thin-disk orbits), while 60% of the EMP stars have highly prograde disk-like orbits (87 stars on thick-disk orbits, 312 stars on thin-disk orbits). These fractions increase further if one also takes the eccentricity of the orbits into account.

In the near future, the astrophysical properties and origin of these stars will be examined further with data from the large-scale Javalambre / Southern Photometric Local Universe Surveys (J/S-PLUS). These surveys include additional narrow/medium-band filters which allow for photometric estimates of C, N, Mg, and Ca abundances, once ongoing calibration efforts are completed. Of importance, it will then be possible to greatly reduce the influence of carbon on the metallicity estimates, which affect our current SMSS/SAGES sample, as  $[C/Fe]$  can be estimated separately from the  $[Fe/H]$ . The accuracy and precision of the derived metallicities will be improved as well.

In order to confirm the elemental-abundance estimates for the VMP/EMP stars with disk-like orbits, we require medium-resolution spectroscopic follow-up for the catalog of  $\sim 7,600$  VMP and  $\sim 400$  EMP stars, and high-resolution follow-up of the most interesting subset of these. The full catalog of VMP/EMP stars with disk-like orbits is listed in the Appendix, and will be made available in the online material. Determinations of age estimates for our candidate VMP/EMP stars would also help to place constraints on their origins. Nevertheless, our present finding that large frac-

tions of VMP/EMP stars are kinematically associated with the rapidly rotating MW disk system (in particular those at low eccentricity) strongly suggests the presence of an early forming “primordial” disk.

The authors express thanks to Deokkeun An for his thoughts and comments on an early version of this paper. We are also grateful to Evan Kirby and Borja Anguiano for their input as well.

The Stellar Abundance and Galactic Evolution Survey (SAGES) is a multi-band photometric project built and managed by the Research Group of the Stellar Abundance and Galactic Evolution of the National Astronomical Observatories, Chinese Academy of Sciences (NAOC).

This work was supported in part from grant PHY 14-30152; Physics Frontier Center/JINA Center for the Evolution of the Elements (JINA-CEE), and from OISE-1927130: The International Research Network for Nuclear Astrophysics (IReNA), awarded by the US National Science Foundation. Y.S.L. acknowledges support from the National Research Foundation (NRF) of Korea grant funded by the Ministry of Science and ICT (NRF-2021R1A2C1008679). Y.S.L. also gratefully acknowledges partial support for his visit to the University of Notre Dame from OISE-1927130: The International Research Network for Nuclear Astrophysics (IReNA), awarded by the US National Science Foundation. Y.H. (Yang Huang) acknowledges support from the National Key R&D Program of China No. 2019YFA0405500 and National Natural Science Foundation of China grants 11903027 and 11833006. Y.H. (Yutaka Hirai) was supported by JSPS KAKENHI Grant Numbers JP22KJ0157, JP20K14532, JP21H04499, JP21K03614, JP22H01259. Numerical computations were in part carried out on Cray XC50 and computers at the Center for Computational Astrophysics, National Astronomical Observatory of Japan. S.X. acknowledges support from the National Natural Science Foundation of China through the project NSFC 12222301. K.T. was supported by the National Natural Science Foundation of China under grant Nos. 12261141689, 12090044 and 12090040. G.Z. acknowledges support by the National Natural Science Foundation of China under grant nos. 11988101 and 11890694.

## REFERENCES

- An, D., & Beers, T. C. 2020, *ApJ*, 897, 39, doi: [10.3847/1538-4357/ab8d39](https://doi.org/10.3847/1538-4357/ab8d39)
- . 2021a, *ApJ*, 907, 101, doi: [10.3847/1538-4357/abccd2](https://doi.org/10.3847/1538-4357/abccd2)
- . 2021b, *ApJ*, 918, 74, doi: [10.3847/1538-4357/ac07a4](https://doi.org/10.3847/1538-4357/ac07a4)
- An, D., Beers, T. C., Lee, Y. S., & Masseron, T. 2023, *ApJ*, 952, 66, doi: [10.3847/1538-4357/acd5cb](https://doi.org/10.3847/1538-4357/acd5cb)
- Baumgardt, H., & Vasiliev, E. 2021, *MNRAS*, 505, 5957, doi: [10.1093/mnras/stab1474](https://doi.org/10.1093/mnras/stab1474)
- Beers, T. C., Norris, J. E., Placco, V. M., et al. 2014, *ApJ*, 794, 58, doi: [10.1088/0004-637X/794/1/58](https://doi.org/10.1088/0004-637X/794/1/58)
- Beers, T. C., Preston, G. W., & Shectman, S. A. 1985, *AJ*, 90, 2089, doi: [10.1086/113917](https://doi.org/10.1086/113917)

- . 1992, *AJ*, 103, 1987, doi: [10.1086/116207](https://doi.org/10.1086/116207)
- Carollo, D., Beers, T. C., Chiba, M., et al. 2010, in *Chemical Abundances in the Universe: Connecting First Stars to Planets*, ed. K. Cunha, M. Spite, & B. Barbuy, Vol. 265, 267–270, doi: [10.1017/S1743921310000724](https://doi.org/10.1017/S1743921310000724)
- Carollo, D., Christlieb, N., Tissera, P. B., & Sillero, E. 2023, *ApJ*, 946, 99, doi: [10.3847/1538-4357/acac25](https://doi.org/10.3847/1538-4357/acac25)
- Carollo, D., Chiba, M., Ishigaki, M., et al. 2019, *ApJ*, 887, 22, doi: [10.3847/1538-4357/ab517c](https://doi.org/10.3847/1538-4357/ab517c)
- Carter, C., Conroy, C., Zaritsky, D., et al. 2021, *ApJ*, 908, 208, doi: [10.3847/1538-4357/abcda4](https://doi.org/10.3847/1538-4357/abcda4)
- Cenarro, A. J., Moles, M., Cristóbal-Hornillos, D., et al. 2019, *A&A*, 622, A176, doi: [10.1051/0004-6361/201833036](https://doi.org/10.1051/0004-6361/201833036)
- Chambers, K. C., Magnier, E. A., Metcalfe, N., et al. 2016, *arXiv e-prints*, arXiv:1612.05560, doi: [10.48550/arXiv.1612.05560](https://doi.org/10.48550/arXiv.1612.05560)
- Christlieb, N. 2003, *Reviews in Modern Astronomy*, 16, 191, doi: [10.1002/9783527617647.ch8](https://doi.org/10.1002/9783527617647.ch8)
- Conroy, C., Naidu, R. P., Zaritsky, D., et al. 2019, *ApJ*, 887, 237, doi: [10.3847/1538-4357/ab5710](https://doi.org/10.3847/1538-4357/ab5710)
- Cordoni, G., Da Costa, G. S., Yong, D., et al. 2021, *MNRAS*, 503, 2539, doi: [10.1093/mnras/staa3417](https://doi.org/10.1093/mnras/staa3417)
- De Silva, G. M., Freeman, K. C., Bland-Hawthorn, J., et al. 2015, *MNRAS*, 449, 2604, doi: [10.1093/mnras/stv327](https://doi.org/10.1093/mnras/stv327)
- Deng, L.-C., Newberg, H. J., Liu, C., et al. 2012, *Research in Astronomy and Astrophysics*, 12, 735, doi: [10.1088/1674-4527/12/7/003](https://doi.org/10.1088/1674-4527/12/7/003)
- Di Matteo, P., Spite, M., Haywood, M., et al. 2020, *A&A*, 636, A115, doi: [10.1051/0004-6361/201937016](https://doi.org/10.1051/0004-6361/201937016)
- Ebeling, H., White, D. A., & Rangarajan, F. V. N. 2006, *MNRAS*, 368, 65, doi: [10.1111/j.1365-2966.2006.10135.x](https://doi.org/10.1111/j.1365-2966.2006.10135.x)
- Fan, Z., Zhao, G., Wang, W., et al. 2023, *ApJS*, 268, 9, doi: [10.3847/1538-4365/ace04a](https://doi.org/10.3847/1538-4365/ace04a)
- Feltzing, S., & Feuillet, D. 2023, *ApJ*, 953, 143, doi: [10.3847/1538-4357/ace185](https://doi.org/10.3847/1538-4357/ace185)
- Fernández-Alvar, E., Kordopatis, G., Hill, V., et al. 2021, *MNRAS*, 508, 1509, doi: [10.1093/mnras/stab2617](https://doi.org/10.1093/mnras/stab2617)
- Gaia Collaboration, Montegriffo, P., Bellazzini, M., et al. 2023, *A&A*, 674, A33, doi: [10.1051/0004-6361/202243709](https://doi.org/10.1051/0004-6361/202243709)
- GRAVITY Collaboration, Abuter, R., Amorim, A., et al. 2020, *A&A*, 636, L5, doi: [10.1051/0004-6361/202037813](https://doi.org/10.1051/0004-6361/202037813)
- Harris, W. E. 2010, *arXiv e-prints*, arXiv:1012.3224, doi: [10.48550/arXiv.1012.3224](https://doi.org/10.48550/arXiv.1012.3224)
- Haywood, M., Di Matteo, P., Lehnert, M. D., et al. 2018, *ApJ*, 863, 113, doi: [10.3847/1538-4357/aad235](https://doi.org/10.3847/1538-4357/aad235)
- Hirai, Y., Beers, T. C., Chiba, M., et al. 2022, *MNRAS*, 517, 4856, doi: [10.1093/mnras/stac2489](https://doi.org/10.1093/mnras/stac2489)
- Huang, Y., Yuan, H., Li, C., et al. 2021, *ApJ*, 907, 68, doi: [10.3847/1538-4357/abca37](https://doi.org/10.3847/1538-4357/abca37)
- Huang, Y., Beers, T. C., Wolf, C., et al. 2022, *ApJ*, 925, 164, doi: [10.3847/1538-4357/ac21cb](https://doi.org/10.3847/1538-4357/ac21cb)
- Huang, Y., Beers, T. C., Yuan, H.-B., et al. 2023, *arXiv e-prints*, arXiv:2307.04469, doi: [10.48550/arXiv.2307.04469](https://doi.org/10.48550/arXiv.2307.04469)
- Keller, S. C., Schmidt, B. P., Bessell, M. S., et al. 2007, *PASA*, 24, 1, doi: [10.1071/AS07001](https://doi.org/10.1071/AS07001)
- Kim, Y. K., Lee, Y. S., Beers, T. C., & Koo, J.-R. 2021, *ApJL*, 911, L21, doi: [10.3847/2041-8213/abf35e](https://doi.org/10.3847/2041-8213/abf35e)
- Koppelman, H. H., Hagen, J. H. J., & Helmi, A. 2021, *A&A*, 647, A37, doi: [10.1051/0004-6361/202039390](https://doi.org/10.1051/0004-6361/202039390)
- Lee, A., Lee, Y. S., Kim, Y. K., Beers, T. C., & An, D. 2023, *ApJ*, 945, 56, doi: [10.3847/1538-4357/acb6f5](https://doi.org/10.3847/1538-4357/acb6f5)
- Li, H., Aoki, W., Matsuno, T., et al. 2022a, *ApJ*, 931, 147, doi: [10.3847/1538-4357/ac6514](https://doi.org/10.3847/1538-4357/ac6514)
- Li, T. S., Ji, A. P., Pace, A. B., et al. 2022b, *ApJ*, 928, 30, doi: [10.3847/1538-4357/ac46d3](https://doi.org/10.3847/1538-4357/ac46d3)
- Limberg, G., Santucci, R. M., Rossi, S., et al. 2021, *ApJ*, 913, 11, doi: [10.3847/1538-4357/abeefe](https://doi.org/10.3847/1538-4357/abeefe)
- Majewski, S. R., Schiavon, R. P., Frinchaboy, P. M., et al. 2017, *AJ*, 154, 94, doi: [10.3847/1538-3881/aa784d](https://doi.org/10.3847/1538-3881/aa784d)
- Mardini, M. K., Frebel, A., Chiti, A., et al. 2022a, *ApJ*, 936, 78, doi: [10.3847/1538-4357/ac8102](https://doi.org/10.3847/1538-4357/ac8102)
- Mardini, M. K., Frebel, A., Ezzeddine, R., et al. 2022b, *MNRAS*, 517, 3993, doi: [10.1093/mnras/stac2783](https://doi.org/10.1093/mnras/stac2783)
- McMillan, P. J. 2017, *MNRAS*, 465, 76, doi: [10.1093/mnras/stw2759](https://doi.org/10.1093/mnras/stw2759)
- Mendes de Oliveira, C., Ribeiro, T., Schoenell, W., et al. 2019, *MNRAS*, 489, 241, doi: [10.1093/mnras/stz1985](https://doi.org/10.1093/mnras/stz1985)
- Onken, C. A., Wolf, C., Bessell, M. S., et al. 2019, *PASA*, 36, e033, doi: [10.1017/pasa.2019.27](https://doi.org/10.1017/pasa.2019.27)
- Placco, V. M., Almeida-Fernandes, F., Arentsen, A., et al. 2022, *ApJS*, 262, 8, doi: [10.3847/1538-4365/ac7ab0](https://doi.org/10.3847/1538-4365/ac7ab0)
- Placco, V. M., Frebel, A., Beers, T. C., & Stancliffe, R. J. 2014, *ApJ*, 797, 21, doi: [10.1088/0004-637X/797/1/21](https://doi.org/10.1088/0004-637X/797/1/21)
- Reid, M. J., & Brunthaler, A. 2020, *ApJ*, 892, 39, doi: [10.3847/1538-4357/ab76cd](https://doi.org/10.3847/1538-4357/ab76cd)
- Rockosi, C. M., Lee, Y. S., Morrison, H. L., et al. 2022, *ApJS*, 259, 60, doi: [10.3847/1538-4365/ac5323](https://doi.org/10.3847/1538-4365/ac5323)
- Rybizki, J., Demleitner, M., Fouesneau, M., et al. 2018, *PASP*, 130, 074101, doi: [10.1088/1538-3873/aabd70](https://doi.org/10.1088/1538-3873/aabd70)
- Santistevan, I. B., Wetzel, A., Sanderson, R. E., et al. 2021, *MNRAS*, 505, 921, doi: [10.1093/mnras/stab1345](https://doi.org/10.1093/mnras/stab1345)
- Schlegel, D. J., Finkbeiner, D. P., & Davis, M. 1998, *ApJ*, 500, 525, doi: [10.1086/305772](https://doi.org/10.1086/305772)
- Schönrich, R., Binney, J., & Dehnen, W. 2010, *MNRAS*, 403, 1829, doi: [10.1111/j.1365-2966.2010.16253.x](https://doi.org/10.1111/j.1365-2966.2010.16253.x)
- Schuster, W. J., Moreno, E., Nissen, P. E., & Pichardo, B. 2012, *A&A*, 538, A21, doi: [10.1051/0004-6361/201118035](https://doi.org/10.1051/0004-6361/201118035)
- Sestito, F., Martin, N., & Starkenburg, E. 2019, in *The Gaia Universe*, 47, doi: [10.5281/zenodo.3236051](https://doi.org/10.5281/zenodo.3236051)
- Sestito, F., Martin, N. F., Starkenburg, E., et al. 2020, *MNRAS*, 497, L7, doi: [10.1093/mnras/slaa022](https://doi.org/10.1093/mnras/slaa022)

- Sestito, F., Buck, T., Starkenburg, E., et al. 2021, MNRAS, 500, 3750, doi: [10.1093/mnras/staa3479](https://doi.org/10.1093/mnras/staa3479)
- Shank, D., Komater, D., Beers, T. C., Placco, V. M., & Huang, Y. 2022, ApJS, 261, 19, doi: [10.3847/1538-4365/ac680c](https://doi.org/10.3847/1538-4365/ac680c)
- Sotillo-Ramos, D., Bergemann, M., Friske, J. K. S., & Pillepich, A. 2023, MNRAS, 525, L105, doi: [10.1093/mnrasl/slad103](https://doi.org/10.1093/mnrasl/slad103)
- Starkenburg, E., Martin, N., Youakim, K., et al. 2017, MNRAS, 471, 2587, doi: [10.1093/mnras/stx1068](https://doi.org/10.1093/mnras/stx1068)
- Steinmetz, M., Zwitter, T., Siebert, A., et al. 2006, AJ, 132, 1645, doi: [10.1086/506564](https://doi.org/10.1086/506564)
- Vasiliev, E. 2019, MNRAS, 482, 1525, doi: [10.1093/mnras/sty2672](https://doi.org/10.1093/mnras/sty2672)
- Venn, K. A., KIELTY, C. L., Sestito, F., et al. 2020, MNRAS, 492, 3241, doi: [10.1093/mnras/stz3546](https://doi.org/10.1093/mnras/stz3546)
- Yanny, B., Rockosi, C., Newberg, H. J., et al. 2009, AJ, 137, 4377, doi: [10.1088/0004-6256/137/5/4377](https://doi.org/10.1088/0004-6256/137/5/4377)
- Yoon, J., Beers, T. C., Placco, V. M., et al. 2016, ApJ, 833, 20, doi: [10.3847/0004-637X/833/1/20](https://doi.org/10.3847/0004-637X/833/1/20)
- York, D. G., Adelman, J., Anderson, John E., J., et al. 2000, AJ, 120, 1579, doi: [10.1086/301513](https://doi.org/10.1086/301513)
- Zepeda, J., Beers, T. C., Placco, V. M., et al. 2023, ApJ, 947, 23, doi: [10.3847/1538-4357/acbbcc](https://doi.org/10.3847/1538-4357/acbbcc)
- Zhao, G., Zhao, Y.-H., Chu, Y.-Q., Jing, Y.-P., & Deng, L.-C. 2012, Research in Astronomy and Astrophysics, 12, 723, doi: [10.1088/1674-4527/12/7/002](https://doi.org/10.1088/1674-4527/12/7/002)
- Zheng, J., Zhao, G., Wang, W., et al. 2018, Research in Astronomy and Astrophysics, 18, 147, doi: [10.1088/1674-4527/18/12/147](https://doi.org/10.1088/1674-4527/18/12/147)



## APPENDIX

Table A1 provides a description of the parameters we report for candidate VMP/EMP stars from the combined SMSS/SAGES sample, based on the information provided by Huang et al. (2022, 2023). Note that we have included photometric-metallicity estimates based on the individual  $u$ -band and  $v$ -band filters, as well as their combination. Note that, for completeness, we have included information for all of the stars with available photometric-metallicity estimates, regardless of their metallicities, errors in their derived metallicities, or reddening. The full table is made available in the online material.

Table A2 is a listing of the candidate VMP/EMP stars on disk-like orbits stars we employ, providing the data needed for further analysis and/or spectroscopic follow-up observations. We have only included stars with adopted photometric-metallicity estimates in the range  $-4.0 < [\text{Fe}/\text{H}] \leq +0.5$ , errors in their adopted metallicities  $\text{err}_{[\text{Fe}/\text{H}]} \leq 0.5$  dex, stars with a difference of less than  $\pm 0.5$  dex between the  $u$ -band and  $v$ -band based abundances ( $|[\text{Fe}/\text{H}]_{\text{ub}} - [\text{Fe}/\text{H}]_{\text{vb}}|$ ), and reddening  $E(B - V) \leq 0.3$ . We also only included stars having derived errors in their orbital rotation velocities  $v_\phi \leq 25 \text{ km s}^{-1}$ , and relative errors in  $Z_{\text{max}} \leq 0.30$  and  $R_{\text{max}} \leq 0.30$ . Note that the listed metallicity errors are internal errors.

Figure A1 compares our photometric-metallicity estimates for VMP/EMP stars to medium- and high-resolution spectroscopic estimates with available  $[\text{Fe}/\text{H}]$  and  $[\text{C}/\text{Fe}]$  (not corrected for evolutionary effects) from a number of literature sources, based on the  $u - G_{\text{BP}}$  colors,  $v - G_{\text{BP}}$  colors, and when available, on the combination of these colors (Huang et al. 2022, 2023). The left column of panels shows the results from the full set of available stars in our catalog regardless of their adopted metallicity errors, while the right column of panels have had the the same cuts applied as listed in the previous paragraph, except where noted below. The top panels apply to matching stars with available  $[\text{Fe}/\text{H}]_{\text{ub}}$ . Note that for the right panel in this row, we have also excluded the stars with  $T_{\text{eff}} \leq 5500 \text{ K}$ , which are the most likely to have metallicity estimates that are affected by carbon enhancement. The middle panels apply to matching stars with available  $[\text{Fe}/\text{H}]_{\text{vb}}$ . The bottom panels apply to matching stars with available  $[\text{Fe}/\text{H}]_{\text{ub+vb}}$ . The right panel in this row only includes stars with  $\text{err}_{[\text{Fe}/\text{H}]_{\text{ub}}} \leq 0.5$  dex,  $\text{err}_{[\text{Fe}/\text{H}]_{\text{vb}}} \leq 0.5$  dex, and  $|[\text{Fe}/\text{H}]_{\text{ub}} - [\text{Fe}/\text{H}]_{\text{vb}}| \leq 0.5$  dex. The dashed lines are the one-to-one lines. In the upper left of each panel, we list the total numbers of stars considered, as well as biweight estimates of the offsets ( $\mu$ ) and dispersions ( $\sigma$ ). The stars with enhanced carbon are indicated by black circles drawn around the symbols.

From inspection of this figure, it is clear that the photometric-metallicity estimates based solely on the  $u$ -band (upper row of panels) are more sensitive to the presence of elevated carbon than are those based solely on the  $v$ -band (middle row of panels). In general, the deviations of the  $u$ -band metallicity estimates are greater, and a larger fraction of the stars are perturbed to higher metallicity than for the  $v$ -band estimates, leading to larger offsets and higher dispersions. Application of the cut on  $T_{\text{eff}} \leq 5500 \text{ K}$  removes a large fraction of the stars that are the most affected by enhanced carbon. As seen from the lower row of panels, the combination of the  $u$ -band and  $v$ -band photometric-metallicity estimates somewhat mitigates the effects of carbon enhancement, resulting in acceptably small offsets and lower dispersions. This motivates our choice to only include stars with photometric-metallicity estimates based on the stars for which acceptable estimates are obtained based either solely on the  $v$ -band or on the combination of the  $u$ -band and  $v$ -band, but excluding stars that have estimates based solely on the  $u$ -band. From this comparison, and under the assumption that the spectroscopic estimates of  $[\text{Fe}/\text{H}]$  (from a number of sources) themselves can account for least a scatter on the order of 0.15 to 0.20 dex, the external errors of the photometric-metallicity estimates range from 0.20 to 0.35 dex (and on the order of 0.10 to 0.15 dex for stars more metal-rich than considered here). Note that this is also driven, at least in part, by scatter induced by the presence of carbon.

Figure A2 provides a comparison of the adopted photometric-metallicity estimates for the stars with available spectroscopic estimates classified as non disk-like (left panel) and disk-like (right panel) stars. From inspection, there appears to be no bias or larger dispersions among the disk-like stars compared to the non disk-like stars.

**Table A1.** Description of the Candidate VMP/EMP Stars in the Combined SMSS/SAGES Sample

Field	Description	Unit
Source ID	The Gaia DR3 Source ID	—
R.A.	The Right Ascension from SMSS DR2 and SAGES DR1 (J2000)	hours : minutes : seconds
Decl.	The Declination from SMSS DR2 and SAGES DR1 (J2000)	degrees : minutes : seconds
$G_C$	The calibration-corrected G magnitude by <a href="#">Huang et al. (2022, 2023)</a> for the Gaia DR3	—
$\text{err}_{G_C}$	The calibration-corrected G magnitude uncertainty by <a href="#">Huang et al. (2022, 2023)</a> for the Gaia DR3	—
BR0	The intrinsic colors of $(G_{BP} - G_{RP})_0$ by <a href="#">Huang et al. (2022, 2023)</a>	—
$\text{err}_{BR0}$	The intrinsic colors uncertainty of $(G_{BP} - G_{RP})_0$ by <a href="#">Huang et al. (2022, 2023)</a>	—
ebv_sfd	The $E(B - V)$ from the extinction map of <a href="#">Schlegel et al. (1998)</a> , corrected by <a href="#">Huang et al. (2022, 2023)</a>	—
$[\text{Fe}/\text{H}]_{\text{ub/vb/ub+vb}}$	The photometric-metallicity estimates from <a href="#">Huang et al. (2022, 2023)</a> .	—
	The “ub”, “vb”, and “ub+vb” indicate the stellar color(s) used in estimating $[\text{Fe}/\text{H}]$ by <a href="#">Huang et al. (2022, 2023)</a>	—
$\text{err}_{[\text{Fe}/\text{H}]_{\text{ub/vb/ub+vb}}}$	The photometric-metallicity estimates uncertainty from <a href="#">Huang et al. (2022, 2023)</a>	dex
$T_{\text{eff}}$	The effective temperature from <a href="#">Huang et al. (2022, 2023)</a>	K
$\text{err}_{T_{\text{eff}}}$	The effective temperature uncertainty from <a href="#">Huang et al. (2022, 2023)</a>	K
dist	The distance from <a href="#">Huang et al. (2022, 2023)</a>	kpc
$\text{err}_{\text{dist}}$	The distance uncertainty from <a href="#">Huang et al. (2022, 2023)</a>	kpc
$\text{flag}_{\text{dist}}$	Flag with “parallax” if the distance is derived by parallax, “CAF”, “CMD.dwarf”, “CMD.dwarf.nobia”, and “CMD-giant” if the distance is derived by color-absolute magnitude fiducial relations from <a href="#">Huang et al. (2022, 2023)</a>	—
RV	The radial velocity from <a href="#">Huang et al. (2022, 2023)</a>	$\text{km s}^{-1}$
$\text{err}_{\text{RV}}$	The radial velocity uncertainty from <a href="#">Huang et al. (2022, 2023)</a>	$\text{km s}^{-1}$
$\text{flag}_{\text{RV}}$	Flag with “GaiaDR3”, “GALAH”, “LM-DR9”, “APG-DR17”, “AEGIS”, “SEGUE”, “Gaia”, “Gaia-ESO”, “LAMOST”, “RAVE”, “LIT”, and “BB” to indicate the source of radial velocity from <a href="#">Huang et al. (2022)</a> , and “GaiaDR3”, “LAMOST”, “SEGUE”, “APOGEE”, “GALAH”, and “RAVE” from <a href="#">Huang et al. (2023)</a>	—
parallax	The parallax from Gaia DR3	mas
$\text{err}_{\text{parallax}}$	The parallax uncertainty from Gaia DR3	mas
pmra	The proper motion in the Right Ascension from Gaia DR3	$\text{mas yr}^{-1}$
$\text{err}_{\text{pmra}}$	The proper motion uncertainty in the Right Ascension from Gaia DR3	$\text{mas yr}^{-1}$
pmdec	The proper motion in the Declination from Gaia DR3	$\text{mas yr}^{-1}$
$\text{err}_{\text{pmdec}}$	The proper motion uncertainty in the Declination from Gaia DR3	$\text{mas yr}^{-1}$
pmra_pmdec_corr	The correlation coefficient between the proper motion in Right Ascension and in Declination from Gaia DR3	—
TYPE	Flag with “Dwarf” and “Giant” from <a href="#">Huang et al. (2022, 2023)</a>	—
SUBTYPE	Flag with “TO” for turn-off stars and “MS” for main-sequence stars from <a href="#">Huang et al. (2022, 2023)</a>	—
$v_\phi$	The rotational velocity as given by AGAMA	$\text{km s}^{-1}$
$\text{err}_{v_\phi}$	The rotational velocity uncertainty as given by Monte Carlo sampling through AGAMA	$\text{km s}^{-1}$
energy	The orbital energy as given by AGAMA	$\text{km}^2 \text{s}^{-2}$
$\text{err}_{\text{energy}}$	The orbital energy uncertainty as given by AGAMA	$\text{km}^2 \text{s}^{-2}$
$J_r/J_\phi/J_z$	The cylindrical actions as given by AGAMA	$\text{kpc km s}^{-1}$
$\text{err}_{J_r/J_\phi/J_z}$	The cylindrical actions uncertainty as given by AGAMA	$\text{kpc km s}^{-1}$
$r_{\text{peri}}$	The Galactic pericentric distance as given by AGAMA	kpc
$\text{err}_{r_{\text{peri}}}$	The Galactic pericentric distance uncertainty as given by AGAMA	kpc
$r_{\text{apo}}$	The Galactic apocentric distance as given by AGAMA	kpc
$\text{err}_{r_{\text{apo}}}$	The Galactic apocentric distance uncertainty as given by Monte Carlo sampling through AGAMA	kpc
$Z_{\text{max}}$	The maximum height above the Galactic plane as given by AGAMA	kpc
$\text{err}_{Z_{\text{max}}}$	The maximum height uncertainty above the Galactic plane as given by Monte Carlo sampling through AGAMA	kpc
$\text{rel}_{\text{err}_{Z_{\text{max}}}}$	The relative uncertainty of the maximum height above the Galactic plane	—
$R_{\text{max}}$	The projection of the Galactic apocentric distance onto the Galactic plane as given by $\sqrt{r_{\text{apo}}^2 - Z_{\text{max}}^2}$	kpc
$\text{rel}_{\text{err}_{R_{\text{max}}}}$	The relative uncertainty of the projection of the Galactic apocentric distance onto the Galactic plane.	—
	The uncertainty is as given by Monte Carlo sampling through AGAMA	—
$I A$	The inclination angle defined as the arctangent ratio of $(Z_{\text{max}} / R_{\text{max}})$	rad
ecc	The eccentricity as given by $(r_{\text{apo}} - r_{\text{peri}}) / (r_{\text{apo}} + r_{\text{peri}})$ through AGAMA	—
criterion	Flag with “ $Z_{\text{max}}$ ”, “Haywood”, or “Both” to indicate the criterion used for the separation of stars on halo-like orbits from those on thick-disk like and thin-disk like orbits	—

**Table A2.** 8,037 VMP/EMP Disk-like Candidate Stars in the Combined SMSS/SAGES Sample

source ID	R.A. (J2000)	Decl. (J2000)	$G_C$	$G_{BP} - G_{RP}$	Type	Dist (kpc)	[Fe/H]	err <sub>[Fe/H]</sub> (dex)	$v_\phi$ (km s <sup>-1</sup> )	$Z_{\max}$ (kpc)	$R_{\max}$ (kpc)	$IA$ (rad)	ecc	criterion
4918300611248859648	00:00:09.07	-59:03:26.0	14.67	0.89	G	2.48	-2.10	0.15	179.3	2.5	7.2	0.33	0.175	Both
2853059333495692800	00:00:18.21	+25:05:15.2	17.99	1.08	D	1.65	-2.01	0.33	160.3	1.3	8.9	0.14	0.317	Both
2853263288606167808	00:00:58.03	+26:00:23.4	17.98	0.99	D	2.76	-2.21	0.33	170.5	2.1	9.4	0.22	0.271	Both
393334518015299456	00:01:58.71	+48:28:56.9	14.87	0.76	D	0.49	-3.01	0.18	289.2	0.2	14.1	0.01	0.266	Both
2880219431068389632	00:02:39.84	+36:50:18.5	17.73	0.87	D	2.14	-2.06	0.35	224.8	1.1	10.1	0.11	0.125	Both
2753212785655871232	00:02:45.20	+09:39:16.7	17.24	0.95	D	2.50	-2.04	0.21	173.4	2.1	8.7	0.24	0.248	Both
393469620510488704	00:03:14.30	+49:05:15.0	16.53	0.65	D	1.02	-2.80	0.49	192.6	0.4	8.8	0.05	0.188	Both
2854920566162852480	00:03:23.78	+28:42:22.8	16.46	1.11	D	1.32	-2.13	0.10	223.1	1.0	9.2	0.11	0.096	Both
2741858266514981120	00:03:28.26	+04:25:45.1	15.67	1.09	D	0.78	-2.10	0.12	215.4	1.3	8.2	0.16	0.056	Both
2421349012110147840	00:03:51.14	-12:31:54.1	12.65	1.03	G	2.77	-2.24	0.06	181.5	3.4	8.9	0.36	0.252	Haywood
2873937856715519360	00:03:59.36	+31:59:28.0	14.69	0.66	D	0.74	-3.24	0.12	228.6	0.5	9.1	0.06	0.089	Both
384033714794591360	00:04:06.01	+41:11:59.4	14.00	0.82	D	1.25	-2.17	0.18	255.7	0.7	12.2	0.05	0.213	Both
2365861363244694400	00:04:33.86	-19:20:07.2	12.74	1.01	G	3.48	-2.38	0.05	161.0	3.6	7.8	0.43	0.255	Haywood
2849652771593602816	00:05:36.71	+23:21:05.2	14.92	0.74	G	2.08	-2.38	0.29	190.8	6.9	10.0	0.60	0.207	Haywood
2336677850742658560	00:06:02.35	-24:20:46.2	12.14	0.72	D	0.49	-2.53	0.29	227.7	1.0	8.8	0.11	0.087	Both
2877216252495963904	00:06:06.32	+36:48:40.0	17.33	0.69	D	2.09	-2.00	0.45	207.1	1.0	9.1	0.10	0.105	Both
2849709804463640192	00:06:40.68	+24:01:55.2	18.13	1.01	D	2.63	-2.01	0.39	177.7	1.8	10.0	0.18	0.299	Both
2740793733100805632	00:06:51.22	+03:21:37.1	13.99	0.89	D	0.46	-2.34	0.04	240.3	8.9	14.3	0.56	0.377	Haywood
2876918628442545152	00:06:55.97	+35:54:29.0	17.50	0.84	D	2.18	-2.70	0.21	190.7	1.0	9.1	0.10	0.171	Both
2546602108275485568	00:06:57.29	+01:15:53.4	17.26	0.72	D	1.83	-2.66	0.20	158.5	1.8	9.4	0.19	0.384	Both
2546576235392174976	00:06:59.39	+00:59:52.4	18.11	0.83	D	2.79	-2.94	0.43	200.2	12.6	18.6	0.60	0.600	Haywood
387011948195243904	00:07:07.26	+46:51:39.2	14.35	0.87	D	0.75	-2.01	0.29	178.0	0.2	9.1	0.03	0.292	Both
2753300196831120896	00:07:40.88	+10:20:18.9	13.68	1.24	G	1.90	-2.01	0.03	187.3	1.5	8.6	0.17	0.183	Both
2319766674712899840	00:07:42.57	-30:56:13.4	11.72	0.96	G	1.57	-2.08	0.04	179.0	2.0	8.2	0.23	0.240	Both
2738973079283594112	00:07:44.09	+02:19:03.5	17.78	0.88	D	2.68	-2.14	0.31	170.8	2.8	10.0	0.28	0.349	Both
2739001632226213504	00:08:36.17	+02:34:11.1	17.26	0.70	D	1.86	-2.53	0.21	162.1	5.9	12.6	0.44	0.513	Haywood
2850303781261314560	00:09:11.97	+25:09:25.9	17.80	0.96	D	2.59	-2.79	0.25	189.0	2.0	9.9	0.20	0.238	Both
2880809078539501952	00:09:18.70	+38:34:50.5	17.60	0.74	D	2.22	-2.30	0.40	194.3	0.9	9.3	0.10	0.168	Both
2443519530213095168	00:09:47.75	-06:15:31.9	17.60	1.01	D	1.66	-2.16	0.14	174.9	1.9	8.4	0.23	0.238	Both
2443550965077613696	00:09:48.23	-05:50:04.3	17.61	1.04	D	2.37	-2.64	0.26	180.2	4.5	8.3	0.49	0.171	Haywood

NOTE—This table is a stub; the full table is available in the electronic edition.

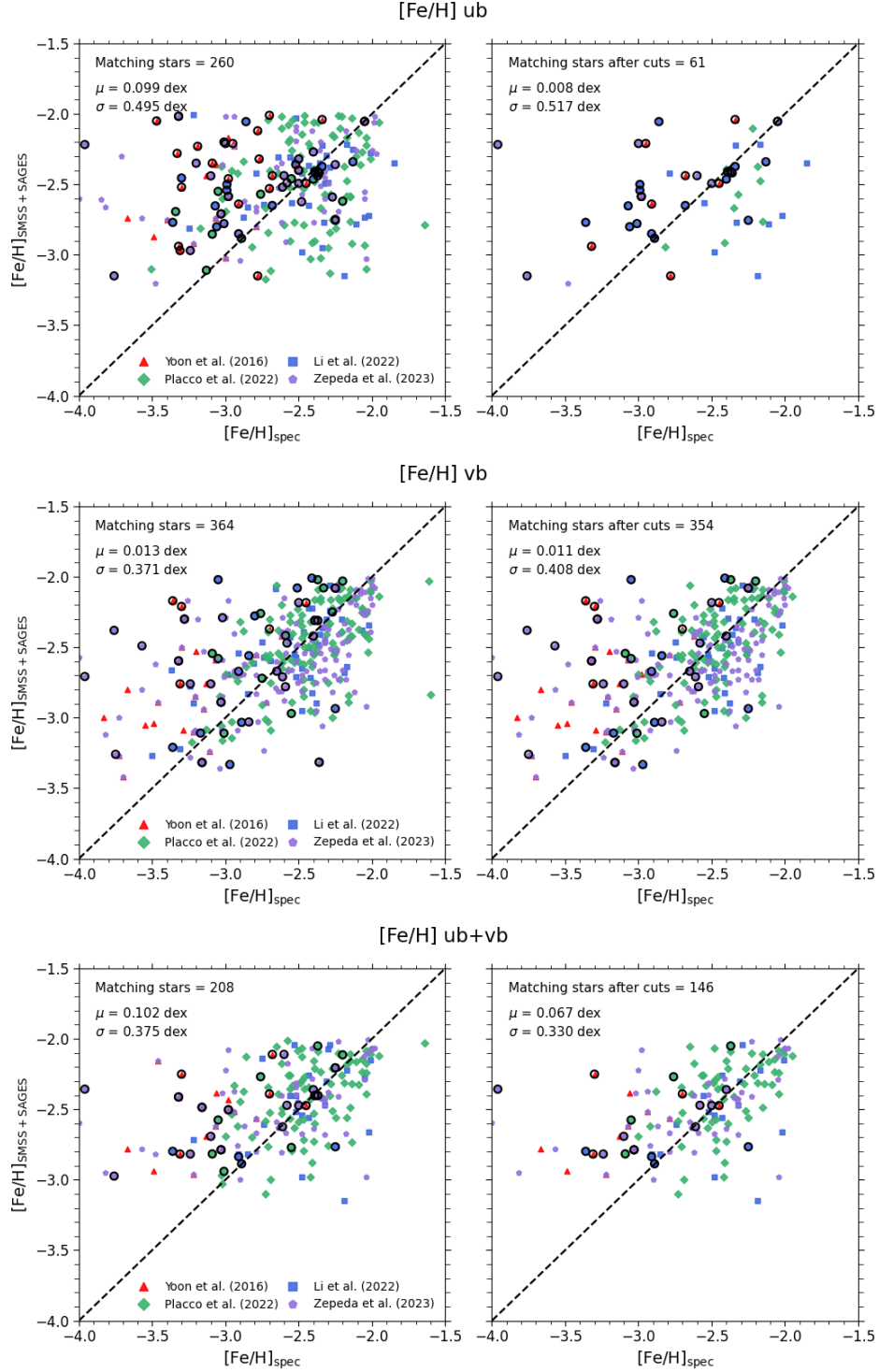


**Figure A1.** Left column of panels: Comparison of the combined SMSS/SAGES photometric-metallicity estimates and spectroscopic metallicities for VMP/EMP stars, based on cross-matches to medium/high-resolution spectroscopic samples with available  $[\text{Fe}/\text{H}]$  and  $[\text{C}/\text{Fe}]$ . The stars from Yoon et al. (2016), Li et al. (2022a), Placco et al. (2022), and Zepeda et al. (2023) are shown as red triangles, blue squares, green diamonds, and purple pentagons, respectively. The black circles indicate carbon-enhanced stars that satisfy  $[\text{C}/\text{Fe}] > +0.7$ . Note that for our present purpose we employ the “as observed”  $[\text{C}/\text{Fe}]$ , without applying evolutionary corrections (e.g., from Placco et al. 2014). From top to bottom, the panels indicate matches for stars with metallicities based on the calibrated  $u - G_{\text{BP}}$  colors,  $v - G_{\text{BP}}$  colors, and when available, on an average of both of these colors (Huang et al. 2022, 2023). The legends in each panel indicate the numbers of matching stars, as well as the biweight location ( $\mu$ ) and scale ( $\sigma$ ) of the metallicity residuals. The dashed line is the one-to-one line. Right column of panels: Comparison with the same spectroscopic catalogs, but after applying a number of cuts (see text). Note that in the right panel of the first row, we have also excluded the stars with  $T_{\text{eff}} \leq 5500$  K.



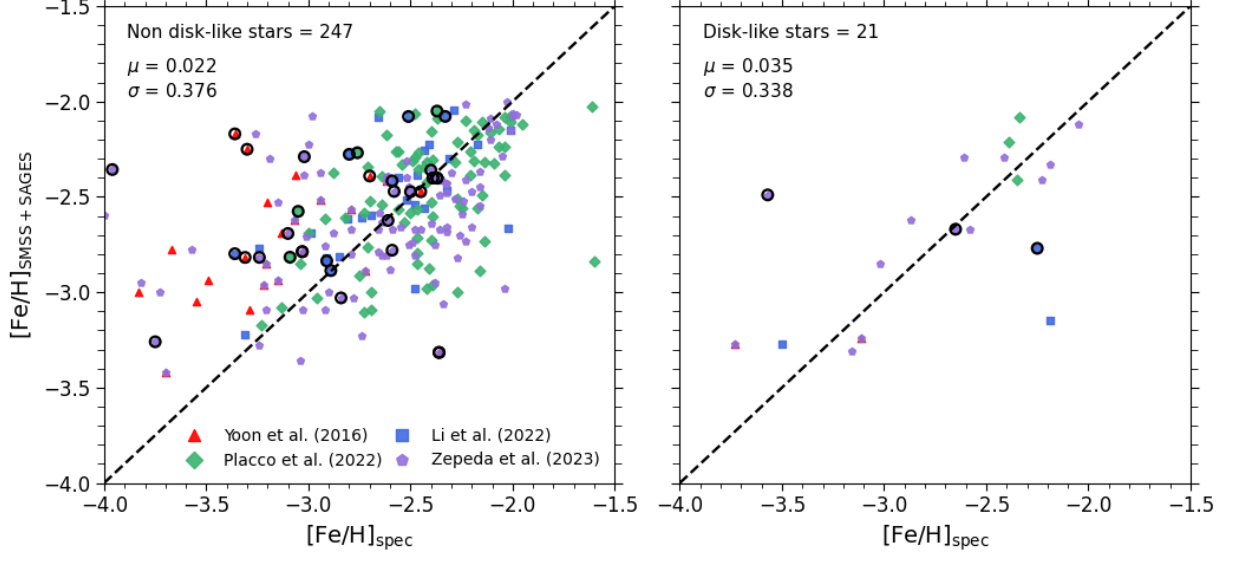


**Figure A2.** Left panel: Similar to Figure A1, but for comparison of the adopted SMSS/SAGES photometric-metallicity estimates and spectroscopic metallicities for VMP/EMP stars classified as non disk-like stars (see text). Right panel: Same, but for stars classified as disk-like stars. The black circles indicate carbon-enhanced stars that satisfy  $[\text{C}/\text{Fe}] > +0.7$ . The legends in each panel indicate the numbers of matching stars, as well as the biweight location ( $\mu$ ) and scale ( $\sigma$ ) of the metallicity residuals. The dashed line is the one-to-one line.